

Journal Pre-proofs

A general model for carbon isotopes in red-lineage phytoplankton: Interplay between unidirectional processes and fractionation by RubisCO

Elise B. Wilkes, Ann Pearson

PII: S0016-7037(19)30566-6
DOI: <https://doi.org/10.1016/j.gca.2019.08.043>
Reference: GCA 11422

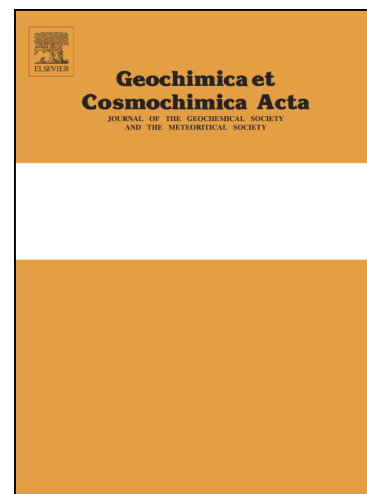
To appear in: *Geochimica et Cosmochimica Acta*

Received Date: 10 April 2019
Revised Date: 29 August 2019
Accepted Date: 31 August 2019

Please cite this article as: Wilkes, E.B., Pearson, A., A general model for carbon isotopes in red-lineage phytoplankton: Interplay between unidirectional processes and fractionation by RubisCO, *Geochimica et Cosmochimica Acta* (2019), doi: <https://doi.org/10.1016/j.gca.2019.08.043>

This is a PDF file of an article that has undergone enhancements after acceptance, such as the addition of a cover page and metadata, and formatting for readability, but it is not yet the definitive version of record. This version will undergo additional copyediting, typesetting and review before it is published in its final form, but we are providing this version to give early visibility of the article. Please note that, during the production process, errors may be discovered which could affect the content, and all legal disclaimers that apply to the journal pertain.

© 2019 Elsevier Ltd. All rights reserved.



A general model for carbon isotopes in red-lineage phytoplankton: Interplay between unidirectional processes and fractionation by RubisCO

Elise B. Wilkes^{a,b*} and Ann Pearson^a

^aDepartment of Earth and Planetary Sciences, Harvard University, Cambridge, MA USA

^bDivision of Geological and Planetary Sciences, California Institute of Technology, Pasadena, CA USA

*ebwilkes@caltech.edu

Abstract

The carbon isotopic composition of organic matter preserved in marine sediments provides a window into the global carbon cycle through geologic time, including variations in atmospheric CO₂ levels. Traditional models for interpreting isotope records of marine phytoplankton assume that these archives primarily reflect kinetic isotope discrimination by the carbon-fixing enzyme RubisCO. However, some *in vivo* and *in vitro* measurements appear to contradict this assumption, indicating that significant questions remain about the mechanistic underpinning of algal isotopic signatures, including the role of carbon concentrating mechanisms (CCMs). Here, we present a general model to explain photosynthetic carbon isotope fractionation (ϵ_p) in marine red-lineage phytoplankton groups; the model reproduces existing chemostat and batch culture datasets with a normalized root mean squared error (nRMSE) of 6.8%. Our framework proposes that a nutrient- and light-dependent step upstream of RubisCO is a kinetic barrier to carbon acquisition and therefore represents a significant source of isotopic fractionation. We suggest this step represents a carbon concentrating strategy that becomes favorable to cells under conditions of excess photon flux. The primary implications are that RubisCO is predicted to exert minimal isotopic control in photon-rich, nutrient-limited regimes but becomes influential as growth becomes light-limited. This framework enables both environment-specific and taxon-specific isotopic predictions. By refining the mechanistic understanding of marine photosynthetic carbon isotope fractionation, we may begin to reconcile existing datasets and reexamine Phanerozoic isotope records—including the resulting CO₂ reconstructions—by emphasizing the influence of different types of resource limitation on photosynthetic carbon acquisition.

1. Introduction

Accurate interpretations of marine organic carbon isotope records rely on a mechanistic understanding of photosynthetic carbon isotope fractionation (ϵ_p). Isotopic models for phytoplankton share the common goal to understand ϵ_p in the context of ambient carbon dioxide concentrations [$\text{CO}_{2(\text{aq})}$] and algal physiology (e.g., Sharkey and Berry, 1985; Laws et al., 1995; Cassar et al., 2006; Schulz et al., 2007; McClelland et al., 2017), thereby enabling efforts to reconstruct $p\text{CO}_2$ (paleobarometry; Jasper and Hayes, 1990; Laws et al., 2002; Pagani et al., 2011). The most widely adopted framework consists of a two-step, passive-diffusive supply model (Rau et al., 1992; Francois et al., 1993; Goericke et al., 1994; Laws et al., 1995; Rau et al., 1996) that was adapted from studies on land plants (Farquhar et al., 1982, 1989). This model predicts that ϵ_p depends on the balance between two processes with distinct isotope effects: diffusion of CO_2 ($< 1\text{‰}$ in water; O'Leary, 1984) and CO_2 fixation by the enzyme RubisCO ($\sim 25\text{--}30\text{‰}$; Table 1). When algal growth rates (μ) are low or ambient CO_2 concentrations are high, the rate-limiting step is presumed to be carbon fixation by RubisCO, and the isotope effect associated with this process sets the theoretical maximum value of ϵ_p , which is denoted ϵ_f (for “fixation”). When instead the supply of CO_2 is rate-limiting, the fractionation accompanying passive diffusion of CO_2 is expressed, defining the minimum value of ϵ_p . These endmembers correspondingly define a line that denotes all intermediate conditions.

Until recently, it has been assumed that the value of ϵ_f equals the fractionation measured *in vitro* for RubisCO from higher plants (Table 1; Roeske and O'Leary 1984; Guy et al., 1993; Scott et al., 2004; McNevin et al., 2006), adjusted slightly for the effects of anaplerotic reactions (β -carboxylations; Francois et al., 1993). This perspective was reinforced by nitrate-limited chemostat experiments with three species of eukaryotic phytoplankton that yielded ϵ_f values of $\sim 25\text{‰}$ at the limit of infinite CO_2 supply or slow growth (Figure 1, Table 1; Popp et al., 1998). However, mounting evidence suggests that this RubisCO-centric framework must be revisited. RubisCO exists in several catalytically and phylogenetically distinct forms in phytoplankton, Forms IA, IB, ID and II (Tabita et al., 2008; Whitney et al., 2011); and in particular, the value of $\epsilon_{\text{RubisCO}}$ for the Form ID version in the haptophyte alga *Emiliania huxleyi* is reported to be only

11‰ (Boller et al., 2011). It now seems incorrect to interpret the *in vivo* ϵ_f values for algal species having Form ID RubisCO by analogy to *in vitro* measurements of Form IB RubisCO from spinach (Rickaby et al., 2015; Wilkes et al., 2017; McClelland et al., 2017).

Indeed, other measurements in addition to Boller et al. (2011) support the suggestion that ϵ_f values inferred from chemostat experiments do not correspond to $\epsilon_{\text{RubisCO}}$ values (Table 1; Figure 1). Form ID RubisCO purified from the diatom *Skeletonema costatum* yields a value of $\epsilon_{\text{RubisCO}}$ of 18.5‰ (Boller et al., 2015). Similarly, recent chemostat incubations with a dinoflagellate employing Form II RubisCO indicate an ϵ_f value of 27‰ *in vivo* (*Alexandrium tamarense*; Wilkes et al., 2017). Although consistent within error estimates with the ~25‰ ϵ_f values for other large “red” plastid lineage algae, this result was surprising given the striking differences in catalytic properties, structures, and amino acid sequences between Form I and II RubisCOs (Rowan et al., 1996) and also the apparent similarities between dinoflagellate and proteobacterial Form II RubisCOs ($\epsilon_{\text{RubisCO}} \approx 18\text{--}23\%$, Form II; Robinson et al., 2003; McNevin et al., 2007). Collectively, the observations indicate that ϵ_f values for eukaryotes from nitrate-limited chemostat experiments are in good agreement *with one another*, yet they consistently do not equal the kinetic isotope effects measured for purified RubisCOs from the most taxonomically similar algal or bacterial source (Figure 1, Table 1).

Several additional lines of evidence support a greater diversity in $\epsilon_{\text{RubisCO}}$ values than previously assumed. Observations of variable $\epsilon_{\text{RubisCO}}$ values are reasonable, because RubisCO’s intrinsic isotope discrimination has been linked empirically and mechanistically to the enzyme’s kinetic properties (Tcherkez et al., 2006). McNevin et al. (2007) demonstrated that a single point mutation in the large subunit of Form IB RubisCO from tobacco had a dramatic effect, lowering the *in vitro* fractionation from 27.4‰ in the wild-type to 11.2‰ in the mutant. Characterization of Form ID RubisCO kinetic properties from 11 diatoms and 3 haptophytes also uncovered unexpected diversity (Young et al., 2016; Heureux et al., 2017). Such diversity makes the uniform ϵ_f value of ~25-27‰ for eukaryotic phytoplankton surprising and suggests the value of ϵ_f could, alternatively, reflect some other common process.

Here we propose a general theoretical model for ϵ_p in marine red-lineage phytoplankton to reconcile the apparent contradictions between ϵ_f values and $\epsilon_{\text{RubisCO}}$ measurements, with the aim of unifying existing data and models. Our model is tested against a wide range of experimental datasets – including both chemostat and batch-culture approaches – and is constructed such that the rate-limiting step for photosynthetic carbon fixation varies depending on the balance of nutrient and light availability. This work builds upon a long history of modeling and culturing efforts that demonstrate the importance of nutrient availability, energy sources, and carbon concentrating mechanisms (CCMs) to the expression of ϵ_p (*e.g.*, Beardall et al., 1982; Tchernov et al., 1997; Burkhardt et al., 1999a,b; Riebesell et al., 2000a,b; Rost et al., 2002, 2006; Cassar et al., 2006; Schulz et al., 2007; Hopkinson, 2014; Hoins et al., 2016; Holtz et al., 2017).

The primary innovation of our model is that under nutrient-limited, light-replete conditions (*e.g.*, chemostat culture experiments; Popp et al., 1998; Wilkes et al., 2017, 2018), we hypothesize that the rate-limiting step occurs upstream of RubisCO and accompanies an irreversible conversion of CO_2 to HCO_3^- . Because this reaction is taken to be the rate-limiting process, and because it is proposed to be common to red-lineage (larger-celled) marine algae, it can provide a constant discrimination against ^{13}C , regardless of taxonomy.

A common upstream process would mask the variable isotope effects associated with RubisCO, unless the cells experience alternate conditions in which RubisCO activity becomes the slow step of carbon fixation. This is proposed to occur under nutrient-replete conditions in which the photon flux rate becomes growth-limiting. We define this as “light-limited”, by which we mean a status of relative limitation and/or the presence of excess nutrients rather than an absolute threshold for a specific photon flux. The implication is that there are two distinct rate-limiting steps for carbon fixation, with different maximum values for ϵ_p at the limit of slow μ and high $[\text{CO}_{2(\text{aq})}]$. Here we relate our generalized model to existing algal physiology models, show how it can explain existing chemostat and batch-culture data, identify plausible cellular mechanisms and evolutionary drivers, and consider the implications for interpreting marine ϵ_p records in the context of paleobarometry.

2. Generic Model for Marine Red-Lineage Phytoplankton

2.1 Biological structure

The model uses a simplified cellular architecture to represent a generic, red-lineage algal cell consisting of a cytosol, a membrane-bound chloroplast, a network of thylakoids, and a pyrenoid where RubisCO is concentrated (Figure 2). The pyrenoid enables buildup of CO_2 around RubisCO and discourages entry and buildup of O_2 , which competitively inhibits CO_2 fixation. The sites of the light reactions of photosynthesis—the thylakoids—are modeled as contacting or penetrating the pyrenoid. Evidence for these physical features is broadly distributed across eukaryotic phytoplankton groups (Badger et al., 1998; Tachibana et al., 2011; Engel et al., 2015; Meyers et al., 2017), with exception of a small number of cases in which the pyrenoid appears to be absent (Ratti et al., 2007; Darienko et al., 2015; Heureux et al., 2017). The internal volume of the thylakoid is acidic, while the chloroplast volume surrounding the thylakoid is alkaline (Raven, 1997; Höhner et al., 2016).

The model includes passive diffusion of CO_2 plus two mechanisms of active carbon acquisition:

- (1) Transport of extracellular HCO_3^- through the plasmalemma and chloroplast membranes using membrane-bound transporters. Within the chloroplast, carbonic anhydrase (CA) equilibrates the HCO_3^- with CO_2 . We call this the “gamma” (γ) pathway.
- (2) Enhanced diffusion or scavenging of CO_2 *via* a putative hydroxylating process that promotes the unidirectional conversion of CO_2 to HCO_3^- . We assume that this process is directly coupled to transport of HCO_3^- across the thylakoid membrane to suppress the reverse reaction and permit accumulation of charged bicarbonate within the thylakoid. This approach would help maintain a CO_2 concentration gradient between the extracellular environment and the chloroplast by drawing down intracellular CO_2 . Kinetic conversion of CO_2 to HCO_3^- would also recapture CO_2 leaking away from the pyrenoid or accumulating within the chloroplast through mechanism (1). In all cases, the final step is the accumulation of CO_2 near RubisCO by dehydration of the captured HCO_3^- by a thylakoid-located CA that penetrates the pyrenoid. We call this the “omega” (ω) pathway.

2.2 Relationship to existing CCM definitions

RubisCO is characterized by a slow maximum catalytic turnover rate and a low affinity for CO₂ (Badger et al., 1998). These inefficiencies are exacerbated in marine environments by the slow diffusion of CO₂ in water and by inorganic carbon speciation favoring HCO₃⁻. Phytoplankton actively regulate the CO₂ concentration around RubisCO with biophysical and biochemical CCMs to ensure efficient fixation (for recent reviews, see Reinfelder, 2011; Griffiths et al., 2017). One implication of this physiology is that the concentration of CO₂ around RubisCO rarely would be predicted to reflect the concentration of CO₂ outside the cell, a prediction supported by field studies of diatoms (Kranz et al., 2015). Another implication is that in the absence of intracellular substructures, the CO₂ diffusive gradient between internal and external environments generally would be inverted (intracellular [CO_{2(aq)}] > extracellular [CO_{2(aq)}]), an impediment to carbon flux unless specific strategies are employed to enhance inward-directed diffusion and/or transport (Raven and Beardall, 2015). The model topology used here was designed to reflect these considerations, including maintaining high CO₂ concentrations around RubisCO (Figure S2).

Our two active carbon acquisition mechanisms synthesize a variety of experimentally-verified CCM components (Table S1) into the two categories of active processes detailed above. In the commonly-invoked CCMs, CO₂ and HCO₃⁻ are assumed to only substantially interconvert in the presence of carbonic anhydrase, *i.e.*, as in the γ pathway (Hopkinson et al., 2016; Mangan et al., 2016). Our model proposes that the ω pathway is a distinct category of CCM: namely, a transmembrane, photon-energized or photosynthetically-enhanced hydroxylation of CO₂ to HCO₃⁻. Unidirectional moieties sharing some of these characteristics have been described or modeled in cyanobacteria, green algae, proteobacteria, and land plants (Vолоkita et al., 1984; Fridlyand et al., 1996; Kaplan and Reinhold, 1999; Tchernov et al., 2001; Wang and Spalding, 2014; Eichner et al., 2015; Griffiths et al., 2017; Desmarais et al., 2019).

Other transport mechanisms for HCO₃⁻ are less quantitatively significant. We assume that HCO₃⁻ does not diffuse through membranes to any significant extent since cell membranes restrict diffusion of

charged species (*e.g.*, Davis, 1958). However, equilibration of HCO_3^- with the uncharged species H_2CO_3 may supply a minor, passive flux of inorganic carbon through membranes (Mangan et al., 2016). Therefore, HCO_3^- is permitted to passively transit the membrane-bound cytoplasm and chloroplast as H_2CO_3 (depicted with dotted arrows in Figure 2) but at a rate approximately four orders of magnitude slower than passive diffusion of CO_2 . Default membrane permeability coefficients for both CO_2 and HCO_3^- (P_C and P_H) were adopted from Hopkinson et al. (2011), a study which analyzed carbon fluxes in diatoms using membrane inlet mass spectrometry and kinetic models of ^{18}O -exchange. Hopkinson et al. (2011) reported permeabilities of $(3.1 \pm 0.4) \times 10^{-2} \text{ cm s}^{-1}$ and $(0.4 \pm 1.0) \times 10^{-6} \text{ cm s}^{-1}$ for *P. tricornutum*. Coefficients optimizing model-measurement agreement were selected from these reported values, within error ($P_C = 2.7 \times 10^{-2} \text{ cm s}^{-1}$ and $P_H = 1.4 \times 10^{-6} \text{ cm s}^{-1}$). For *E. huxleyi*, a lower permeability coefficient for CO_2 was used ($P_C = 0.85 \times 10^{-2} \text{ cm s}^{-1}$).

2.3. Steady-state flux and isotope balance model

We developed a carbon isotope and flux-balance model following the reaction network approach of Hayes (2001). The model is described by coupled, first-order differential equations which are solved for steady-state fluxes (ϕ), intracellular concentrations of CO_2 and HCO_3^- , and $\delta^{13}\text{C}$ values using the ODE23s integrator in Matlab R2018a (SI Equations 1–10, 32–44; Figure S1). The isotope flux balance includes 11 carbon pools with defined isotopic compositions and masses, and 26 distinct fluxes between these pools (Figure S1; Table S3).

The model includes two tunable parameters to govern the fluxes through the hypothesized hydroxylation pathway (ω) and through the bicarbonate transporters (γ). Assigned constants include the rate constants for uncatalyzed and catalyzed interconversions of CO_2 and HCO_3^- , permeability coefficients governing the passive transfer of CO_2 and HCO_3^- through membranes, and intracellular compartment pH values (Table S2). Empirical inputs are instantaneous growth rates, particulate organic carbon content per cell, cell surface areas and volumes, and the concentrations of CO_2 and HCO_3^- in the seawater medium

(literature data compiled in Tables S5–S8). Thus, photosynthesis is prescribed in our model by experimental values, rather than being dynamically determined as a function of $[\text{CO}_{2(\text{aq})}]$ in the pyrenoid. Modeled concentrations of CO_2 and HCO_3^- in each compartment (from solving SI Equations 1–10 to steady-state) result from steady-state fluxes between carbon pools. Parameterization of these fluxes is discussed briefly, below, and in detail in SI Section S3.

Under conditions of excess light energy, we assume that extra membrane potential is directed to hydroxylating CO_2 to HCO_3^- . Photon fluxes exceeding the requirement to synthesize biomass may intensify the pH gradient across the thylakoid membrane, with the light-induced transfer of H^+ from water accompanied by diversion of OH^- for the active hydroxylation of CO_2 . This process of OH^- -scavenging could serve a photoprotective function or aid intracellular pH regulation, with carbon concentration representing an ancillary benefit (see Discussion). Thus, this mechanism is assumed to occur constitutively (*i.e.*, even when CO_2 is abundant) under nutrient-limited, high-photon conditions, as its primary role would be to dispose photosynthetically-driven pH gradients. As the balance of energy and nutrients shifts such that nutrients are no longer limiting (light begins to limit growth), we assume that this strategy is less induced. Instead, passive diffusion of CO_2 into the pyrenoid will be the dominant mechanism by which CO_2 accumulates around RubisCO. Thus, diffusion is predicted to be the sole mode of CO_2 entry into the pyrenoid in the limit of minimum photon flux.

We define omega as a unitless parameter (ω ; SI equations 27, 30, 31) to index the balance between energized (*HYD*) or passive ($F_{\text{ce-c}}$; Figure S1) entry of CO_2 into the pyrenoid. This allows us to smoothly adjust the model fluxes between the endmember physiological states of relative nutrient limitation *vs.* relative light limitation. Its influence on the fluxes *HYD* and $F_{\text{ce-c}}$ is approximated by Equation 1 (for a complete definition, see SI). Values of ω approaching 1 imply that CO_2 entry into the pyrenoid occurs entirely *via* the hydroxylation mechanism, while values approaching 0 imply passive diffusion of CO_2 is the exclusive mode of entry into the pyrenoid.

$$\omega \approx \frac{HYD}{HYD + F_{\text{ce-c}}} \quad (1)$$

Active HCO_3^- uptake at the cell and chloroplast boundaries (U ; Figure S1) is permitted by the model, but not required; it is treated as a tunable rate. The cell is assumed to employ active uptake processes (both HYD and U) as a fixed proportion (γ) of the carbon fixation rate (FIX) for a given taxon and growth condition (Equation 2). Thus, the relative flux through the membrane-bound HCO_3^- transporters (U) depends on γ , HYD , and FIX , rather than being a constant value. This parameterization implies that when ω approaches 1 and HYD is maximized, less of the cellular carbon demand will be met through active HCO_3^- import, since the ω hydroxylation pathway is itself a form of CCM. When ω approaches 0 (meaning HYD is absent), import of HCO_3^- will supply more of the actively-acquired inorganic carbon because it will be the only available CCM in the cell.

$$\gamma = \frac{(U + HYD)}{FIX} \quad (2)$$

2.4. Kinetic isotope effects

The model approximates the kinetic isotope effects (ϵ) for all carbon transformations as the difference between δ values (Hayes, 2001). The model includes isotope effects for RubisCO, carbonic anhydrase, and the kinetic hydroxylation and dehydroxylation of CO_2 and HCO_3^- , respectively. These isotope effects are denoted $\epsilon_{\text{RubisCO}}$, ϵ_{HC} , ϵ_{CH} , ϵ_{HYD} , and ϵ_{DEHYD} and are summarized in Table S3.

The isotope effect associated with RubisCO ($\epsilon_{\text{RubisCO}}$) is assigned a value between 11.1 and 19.5‰ depending on the taxonomic identity of the modeled cell (Table 1). For experiments with coccolithophores and diatoms, taxon-specific $\epsilon_{\text{RubisCO}}$ values are available and are adopted directly from the literature (11.1‰ and 18.5‰, respectively, Table 1). The isotope effect for dinoflagellate Form II RubisCO has not been measured, so dinoflagellates are assumed to have an $\epsilon_{\text{RubisCO}}$ value of 19.5‰, falling within the ranges measured for other taxa employing Form II RubisCO, *R. rubrum* and the *Riftia pachyptila* endosymbiont (Table 1).

The isotope effect adopted for the unidirectional conversion of CO_2 to HCO_3^- (ϵ_{HYD}) is 25‰. This choice implies an isotope effect of 34‰ for the reverse process (the unidirectional formation of CO_2 from HCO_3^- , ϵ_{DEHYD} , Table S3) because the forward and reverse reactions must be related by the equilibrium fractionation ($\sim 9\%$ at 25°C ; Zhang et al., 1995; Zeebe, 2014). Several experimental and theoretical studies have attempted to determine the uncatalyzed, kinetic (abiotic) fractionation during hydration or hydroxylation of CO_2 to HCO_3^- which might serve as a guideline or bound on these assumptions (Table S4). Unfortunately, the available data are inconsistent. The most widely-adopted values for the hydration of CO_2 is 13‰ (O’Leary et al., 1992; Zeebe and Wolf-Gladrow, 2001). However, the primary reference for this value is an experimental study reporting a fractionation of only 6.9‰ for the hydration of CO_2 (Marlier and O’Leary, 1984). Thus, two values have been cited in reference to the same study, with no explanation for the contradiction (*c.f.*, Zeebe, 2014). Furthermore, all other reported values from experiments and theoretical calculations are larger than 13‰, so we assume that this value, and the 11‰ value reported by the same group for the analogous hydroxylation reaction, may reflect a problem with back-reactions during their experiments. Reversibility (equilibration) is difficult to prevent and would tend to reduce the expression of the isotope effect (Sade and Halevy, 2017). Once these numbers are taken out of consideration, we select 25‰ as the most parsimonious value, falling within the $\sim 20\text{--}39\%$ range theorized for abiotic hydration and hydroxylation reactions based on experiments by other groups and *ab initio* calculations using transition state theory (Table S4; Siegenthaler and Munnich, 1981; Usdowski et al., 1982; Clark and Lauriol, 1992; Zeebe and Wolf-Gladrow, 2001; Zeebe, 2014). A similar value (30‰) was employed in a carbon-flux study for *Trichodesmium* as a potential fractionation accompanying the cyanobacterial NDH-1₄ complex, which is also thought to hydrate or hydroxylate CO_2 through a potentially irreversible mechanism (Eichner et al., 2015).

2.5. Model implementation

Experimental data for diatoms (2 species), coccolithophores (calcifying and non-calcifying strains), and dinoflagellates (2 species within the same genus) were compiled from the literature (Tables S5–S8). These include nutrient-limited chemostat experiments consolidated from seven sources (Bidigare et al., 1997; Laws et al., 1997; Popp et al., 1998; Cassar, 2003; Hoins et al., 2016; Wilkes et al., 2017, 2018), as well as batch cultures of the same species, compiled from an additional seven sources (Burkhardt et al., 1999a,b; Riebesell et al., 2000a,b; Rost et al., 2002; Hoins et al., 2015, 2016).

Empirical model input parameters were defined according to measurements reported in these studies (Tables S5–S8) and include the instantaneous growth rate (μ_i), corresponding to carbon fixation during the photoperiod (Riebesell et al., 2000a, b), and the particulate organic carbon per cell (POC). Together, these two inputs define the carbon-specific growth rate, $FIX = \mu_i \text{POC}$, which accounts for differences in diel cycle and cellular carbon content between studies (Rost et al., 2002). Experiment-derived inputs also include cell surface area (SA), the concentrations of CO_2 and HCO_3^- in the medium, and reported ε_p values. In some cases, detailed in Tables S5–S8, these inputs were calculated using empirical relationships when direct measurements were not reported.

3. Results

3.1 Behavior of the generalized model for ε_p

First, we demonstrate the general behavior of the model (Figures 3, 4; Figures S3–5) by examining its isotopic endmembers and their underlying physiology. Figure 3 presents several example scenarios using parameters for the coccolithophore, *E. huxleyi*, to show how net fluxes and resulting ε_p values correspond to different conditions of ω , γ , and $[\text{CO}_{2(\text{aq})}]$ (see also Figures S3 and S4). In all scenarios depicted, the concentration of CO_2 in the pyrenoid either is similar to, or significantly exceeds, external $[\text{CO}_2]$. Furthermore, the concentrations in the pyrenoid can be enhanced beyond external $[\text{CO}_2]$ in all scenarios by increasing the active uptake of bicarbonate into the cell (parameter γ). Figure 4 presents the

full model ε_p response for the dinoflagellate, *A. tamarense*, as well as for *E. huxleyi*, over a range of $\mu/[\text{CO}_{2(\text{aq})}]$ conditions. The ε_p response for the diatom, *P. tricornutum*, is shown in Figure S5.

Under high light, nutrient-limited growth, the model generates intercepts of 25‰ for all taxa because this number reflects the full expression of the isotope effect associated with the hydroxylation mechanism (condition **d**, Figure 3; Figure 4). Physiologically, this endmember represents slow μ and/or high $[\text{CO}_{2(\text{aq})}]$, under conditions of high photosynthetic activity ($\omega = 1$). This intercept manifests when virtually all the CO_2 entering the chloroplast leaks back out again, permitting continuous replenishment of $^{12}\text{CO}_2$ around the hypothesized hydroxylating enzyme.

By contrast, the model predicts a diversity of maximum ε_p values during nutrient-replete growth under conditions of light limitation ($\omega < 1$), such as in batch culture experiments. When μ is slow (corresponding to the lowest photon flux densities, PFD, $\mu\text{E m}^{-2} \text{s}^{-1}$), condition **a** (Figure 3) reflects the full expression of the isotope effect associated with each taxon-specific RubisCO, and different taxa are predicted to have different intercepts (Figure 4). In this scenario, CO_2 enters the pyrenoid solely by passive diffusion, and subsequently most leaks out, again due to slow growth (μ) and/or high $[\text{CO}_{2(\text{aq})}]$.

As the ratio $\mu/[\text{CO}_{2(\text{aq})}]$ increases (conditions **b**, **c**, and **e**, Figure 3; Figure 4), the slope and curvature of the ε_p relationship reflect the ratio of inorganic carbon leaking from the chloroplast relative to the gross inorganic carbon flux into the chloroplast. If CO_2 enters and leaves by diffusion alone, ε_p is a linear function of the ratio $\mu/[\text{CO}_{2(\text{aq})}]$. Because $[\text{CO}_{2(\text{aq})}]$ in the chloroplast equals $[\text{CO}_{2(\text{aq})}]$ outside the cell, ε_p solely reflects the balance between two rate-limiting steps with distinct kinetic isotope effects: passive diffusion of CO_2 in water ($\sim 0\text{‰}$) and either fixation by RubisCO (11-30‰, Table 1) or hydroxylation by *HYD* (25‰, Table S3). If instead active pumping of HCO_3^- into the cell is significant (a relatively high γ value), ε_p is a curvilinear function of the ratio $\mu/[\text{CO}_{2(\text{aq})}]$ because dehydration of HCO_3^- in the chloroplast changes the internal concentration of CO_2 compared to the extracellular environment. When external $[\text{CO}_{2(\text{aq})}]$ is low, $[\text{CO}_{2(\text{aq})}]$ in the chloroplast is higher (as enabled by HCO_3^- import and subsequent equilibration using CA), and a larger fractionation is expressed than would be predicted based on passive diffusion alone. In both

cases, however, the most important control on ε_p is whether the standing stock of CO_2 inside the chloroplast (but external to the thylakoids and pyrenoid) experiences RubisCO or HYD as the rate-limiting step, and how much of this CO_2 subsequently leaks out of the cell—not whether the carbon atoms fixed into biomass were originally sourced from a pool of HCO_3^- versus CO_2 .

The predicted isotopic behavior also is influenced by the permeability coefficients for CO_2 and HCO_3^- (P_C and P_H ; Figure 4). Adjusting P_C and P_H would influence the trajectory of ε_p values when plotted as a function of μ_i/CO_2 in a manner similar to adjusting the value of γ (compare dashed vs. solid lines in Figure 4). Thus, either permeabilities or active import of bicarbonate could be treated as tunable parameters in our model. We treat P_C and P_H as fixed parameters, constrained by measurements of passive (dark) fluxes in the diatom *P. tricornutum* (Hopkinson et al., 2011) to minimize the degrees of freedom in the model.

3.2 Simulation of chemostat and batch culture data

Figures 5–8 show model fits to literature data. Experiments were included only where growth was limited specifically by nitrate or phosphate (Bidigare et al., 1997; Laws et al., 1997; Popp et al., 1998; Cassar, 2003; Hoins et al., 2016; Wilkes et al., 2017, 2018) or light (Burkhardt et al., 1999a,b; Riebesell et al., 2000a,b; Rost et al., 2002; Hoins et al., 2015, 2016), rather than another resource. Species were selected if both nutrient-limited chemostat and light-limited batch culture data were available; the exception is *P. glacialis*, for which there are no batch culture experiments for comparison. The batch culture data were sorted further into groups based on light intensity and diel cycle length (separated by lines in Tables S4–S7).

When μ_i , $[\text{CO}_{2(\text{aq})}]$, $[\text{HCO}_3^-]$, POC, and SA are known from experiments, the only free parameters in the model are ω and γ . To simulate the data, ω and γ were optimized for each experiment (nutrient availability, light intensity, and diel cycle combination) to minimize the sum of the squared residuals between modeled and measured ε_p values. We emphasize that these parameters were optimized by experimental condition rather than data point by data point: a single value of γ was selected for a given

species and growth rate limiting resource (*e.g.*, all experiments with *P. tricornutum* grown in light-limited batch cultures are represented by a single value of γ). Values of ω were permitted to vary between 0 and 1 and were optimized by light condition (*e.g.*, all experiments with *E. huxleyi* grown at PFD = 80 and a 16:8 L:D cycle are fitted using a single value of ω). The optimal values of ω generally increase with increasing photon flux density and daylength for each taxon (Figures 5–8). All resulting fits for ω and γ are reported in Table S9 and in the captions for Figures 5–8.

More data are available for the diatom *P. tricornutum* ($n = 66$) and the haptophyte *E. huxleyi* ($n = 56$) than for other taxa. These are also the datasets that yielded the best agreement between modeled and measured ε_p values (Figures 5 and 6). The model reproduces the curvature of the ε_p values for the *P. tricornutum* chemostat experiments with respect to $\mu_i/[\text{CO}_{2(\text{aq})}]$ (Figure 5b) and the steeper ε_p responses of the more strongly light-limited batch cultures (Figure 5e). It predicts that active HCO_3^- import will comprise 0.6 – 52% of the gross carbon fluxes entering at the cell boundary for the chemostat experiments and 3 – 44% for the batch cultures (Figure S6). For *E. huxleyi*, the model predicts ε_p values in good agreement with all datasets (Figure 6), except it fails to fully reproduce the shallow slope of the lowest light condition (PFD = 30; 16:8; $n = 4$; modeled $\omega = 0.70$). The model predicts a gross HCO_3^- import of 0.8 – 3.8% for the *E. huxleyi* chemostat experiments, and a range of 5 – 51% for the batch cultures (Figure S6).

The taxa with smaller data sets (*Alexandrium spp.*, $n = 13$ and *P. glacialis*, $n = 7$) show poorer agreement between modeled and measured ε_p values (Figures 7 and 8). The model effectively reproduces 7 of the 9 data points from nitrate-limited chemostat cultures of *Alexandrium*. The model does not require any HCO_3^- import to explain the *Alexandrium* chemostat experiments, but it can accommodate low levels of gross HCO_3^- import (< 10%) and still produce reasonable model fits. The model predicts HCO_3^- import of 10 – 49% of the gross carbon influx for the batch cultures of *Alexandrium* (Figure S6). For *P. glacialis*, bicarbonate import is predicted to account for 10 – 44% of the gross carbon fluxes entering the cell (Figure S6).

3.3 Assessing model performance

The model is most effective at predicting ε_p values for *E. huxleyi*, with a normalized root mean squared error (nRMSE) of 6.4% across all batch and chemostat culture data ($n = 56$). The combined *P. tricornutum* datasets ($n = 66$) also are reproduced well (nRMSE of 7.2%). The full set of *Alexandrium* experiments has a larger error (nRMSE of 22.5%) but omitting the two outliers brings this error down to 5.2%. The model is least effective at predicting ε_p values for *P. glacialis* (nRMSE of 25.9%). Among the combined data ($n = 140$; after excluding the two *Alexandrium* outliers), the greatest deviation between modeled and empirical ε_p is an 8.6‰ overestimation for one of the chemostat experiments with *P. glacialis*. Overall, the model reproduces the 140 experiments with an average nRMSE of 6.8% and $R^2 = 0.89$ (Figure 9). The model is best at predicting ε_p values at low and intermediate values of the ratio $\mu/[\text{CO}_{2(\text{aq})}]$. It is less effective at predicting ε_p values in the higher ranges of $\mu/[\text{CO}_{2(\text{aq})}]$, possibly because in these ranges growth rates are actually limited by CO_2 availability rather than light or nutrient delivery, representing a distinct physiological state not encompassed by our model.

4. Discussion

While molecular and physiological evidence indicates that phytoplankton deploy a wide range of CCMs to ameliorate the kinetic limitations of RubisCO, the details of these mechanisms, their isotopic expression under natural environmental conditions, and their relevance to geochemical signatures of global carbon cycling are still debated (Reinfelder, 2011, Matsuda et al., 2011, Bolton and Stoll, 2013, Pagani 2014, Hopkinson et al., 2016, Stoll et al., 2019). Here we assume that the dominant processes influencing organic carbon signatures in marine red-lineage phytoplankton can be captured by a single, simplified carbon isotope flux-balance model, because in chemostat culture studies, representatives from three red-lineage clades with different RubisCOs and life strategies (including presence and absence of biomineralization) display similar isotopic responses to $\mu/[\text{CO}_{2(\text{aq})}]$ (Figure 1). Our model posits the importance of a catalyzed process capable of drawing down intracellular CO_2 to maintain an inward-directed diffusional gradient and/or to channel inorganic carbon directly to RubisCO in the pyrenoid. We

further suggest that this mechanism is distinct from a conventional carbonic anhydrase (CA), and instead propose it is intimately coupled to the thylakoid and its associated, photosynthetically-activated membrane potential.

The primary advantage of such a framework is its ability to explain four major observations: (1) ϵ_f values, inferred from the intercepts of *in vivo* measurements, do not match *in vitro* measurements of $\epsilon_{\text{RubisCO}}$, (2) ϵ_p values respond to cellular surface area and volume (SA/V), consistent with a primarily diffusive mode of CO₂ acquisition and loss from/to the extracellular environment, (3) the availability of nutrients and light affects the expression of ϵ_p , and (4) virtually all eukaryotic phytoplankton taxa are known to use CCMs. Therefore, it can provide a simple and general mechanistic explanation for why—in aggregate—algal paleobarometry has a largely taxon-independent response (*e.g.*, Plancq et al., 2012, Witkowski et al., 2018).

4.1 Influence of light and nutrient conditions on ϵ_p

A variety of light- and nutrient-dependent mechanisms previously have been invoked to explain the variable responses of ϵ_p between chemostat (nutrient-limited) and batch (light-limited) culture conditions. The largest values of ϵ_p (25-27‰) occur in chemostat experiments. It has been suggested that complementary light-limited batch experiments may converge with these data (*i.e.*, form a single curve) after accounting for variations in instantaneous- and cell-specific growth rates (Rost et al., 2002). However, for most datasets, differences persist even after applying these corrections, and thus there must be other influences on ϵ_p .

One additional factor may be the proportion of cyclic to linear electron flow. Large ϵ_p values had been interpreted to result from CO₂ saturation and leakage around a RubisCO with a large ϵ_f value (~25 to 27‰; *e.g.*, Popp et al., 1998, Riebesell et al., 2000a, Cassar et al., 2006, Hoins et al., 2016), where CO₂ saturation was thought to be promoted by an undefined, but ATP-dependent, CCM (Riebesell et al., 2000a, Cassar et al., 2006). Because relative ATP levels are enhanced through cyclic electron flow, large ϵ_p values have been explained as resulting from an ATP-driven, CO₂-pumping CCM localized to the chloroplast

(Riebesell et al., 2000a, Cassar et al., 2006). However, this explanation warrants re-examination due to the recent discovery that cyclic electron flow contributes negligibly to photosynthesis and the regulation of ATP/NADPH in diatoms (Baullier et al., 2015). It also warrants re-examination because $\epsilon_{\text{RubisCO}}$ is not 25 to 27‰ for any of the planktonic taxa measured to-date.

Instead, rates of active carbon acquisition (net CCM-like activity) are known to be enhanced by light and thus responsive to the balance of energy and nutrients (*e.g.*, Hopkinson et al., 2011, 2014; Yamano et al., 2010; Mitchell et al., 2014, 2017). Such regulation has been proposed to mediate the expression of ϵ_p (*e.g.*, Hopkinson et al., 2011; Hopkinson, 2014). Our generalized model adapts and simplifies this idea by introducing the parameter ω to quantify a postulated light-dependent hydroxylation. Its unidirectional nature and physiological association with the thylakoid membrane imply that such a “photo-CCM” directly connects the light reactions of photosynthesis with the dark reactions of CO₂ fixation.

4.2 Reconciling existing CCM models: cellular mechanisms and evolutionary pressures

A generalized strategy of photocatalytic hydroxylation is plausible among red-lineage eukaryotic phytoplankton because light-dependent pH gradients within cells provide uniform physiological pressures that could support the convergent evolution of enzymes and/or cofactors catalyzing this process. When cells are illuminated, an electric field is generated across the thylakoid membrane. While this gradient is used by ATP synthase to produce ATP, an additional, direct role in carbon concentrating mechanisms also has been speculated (Pronina and Borodin, 1993; Raven, 1997, 2014; Thoms et al., 2001; Moroney and Ynalvez, 2007; Kikutani et al., 2016; Holtz et al., 2017; Matsuda et al., 2017). The alkaline chloroplast stroma is naturally suited for hydroxylation reactions, while the acidic thylakoid lumen and its proximity to the pyrenoid would favor protonation and dehydration of accumulated HCO₃⁻ near RubisCO (Raven, 1997; Thoms et al., 2001; Sinetova et al., 2012). This possibility is supported by the recent discovery of lumen-localized, θ -CAs in diatoms (Kikutani et al., 2016), which are analogous to the α -CAs found in the lumen of freshwater green algae (Table 2) and suggest convergent evolution of CCM function of the thylakoid

lumen among eukaryotic phytoplankton (Matsuda et al., 2017; Tsuji et al., 2017; Griffiths et al., 2017). Moreover, a thylakoid-energized CCM would take advantage of an intrinsic feature of oxygenic photosynthesis: namely, it would allow cells to exploit their access to an unlimited supply of electron donor to simultaneously improve their ability to access carbon.

Light-enhanced carbon fluxes are known in other contexts. Light-enhanced calcification is well-established for corals and foraminifera (Cohen et al., 2016) and has been documented for *E. huxleyi* (Barcelos e Ramos et al., 2012). Carbonate production and calcification are thought to serve as supplementary pathways, used to dissipate electrochemical gradients that are generated when excess light is harvested. Similarly, photorespiration appears to respond to excess light in plants and phytoplankton (Parker et al., 2004). These examples point to the universality of light involvement in regulating carbon fluxes within cells.

Another driver for the evolution of a photo-CCM may be protection from photodamage. Cells have evolved numerous strategies to deal with excess photon flux, and these strategies may include enhanced active uptake of HCO_3^- or the energized interconversion of HCO_3^- and CO_2 specifically to consume excess ATP or proton gradients (Tchernov et al., 1997, 2001, 2003; Kaplan and Reinhold, 1999; Tchernov and Lipschultz, 2008; Eichner et al., 2015). Kaplan and Reinfeld (1999) speculate that these energy disposal mechanisms could have originated early in phytoplankton evolution before decreases in CO_2 levels became physiologically limiting and were only subsequently adapted for carbon acquisition. An ancient origin could explain why this energized mechanism could exist within multiple eukaryotic clades.

By contrast, spontaneous reaction cannot be invoked directly as the source of a unidirectional source of HCO_3^- to the thylakoid lumen (Zeebe and Wolf-Gladrow, 2001; Schulz et al., 2006; Mangan et al., 2016). The abiotic hydroxylation of CO_2 is kinetically very slow, with a rate constant for the uncatalyzed conversion of CO_2 to HCO_3^- of $4 \times 10^{-2} \text{ s}^{-1}$ (298.15 K, Salinity = 35; Schulz et al., 2006), *ca.* 10^6 slower than a typical carbonic anhydrase (Bundy, 1986; Hopkinson et al., 2011). Thus, our model proposes that CO_2 import and conversion to HCO_3^- by the photo-CCM must be catalyzed.

One possibility is that this process occurs *via* non-enzymatic catalysis (Keller et al., 2015), a strategy that might be more favorable for the cell when nitrogen for protein synthesis is scarce. However, the more likely possibility is that non-enzymatic catalysis has provided a template for the selective evolution of enzymes. In *Chlamydomonas*, the LCIB/LCIC protein complex structurally resembles a β -CA (Jin et al., 2016). This complex is hypothesized to convert CO_2 to HCO_3^- , potentially with active regulation that minimizes subsequent dehydration (Wang and Spalding, 2014; Jin et al., 2016). Cyanobacteria also have an analogous strategy. The NAD(P)H dehydrogenase (NDH-1) complexes of cyanobacteria are essential for CO_2 uptake, are coupled to cyclic electron flow around photosystem I, and are expressed in a light-dependent manner (Ogawa, 1992; Ogawa and Mi, 2007). Some of these complexes are thought to catalyze the conversion of CO_2 to HCO_3^- (Volokita et al., 1984; Kaplan and Reinhold, 1999; Tchernov et al., 2001; Eichner et al., 2015), potentially rendering the process irreversible through the transport of a proton across the thylakoid membrane (Maeda et al., 2002; Price et al., 2002; Zhang et al., 2004). Unlike in our model, cyanobacteria appear to exhibit no physical cooperation between the thylakoid and the cyanobacterial analogue of the pyrenoid—the carboxysome—so the resulting HCO_3^- accumulates in the cytosol. This difference in cellular architecture may help to explain why the cyanobacterium *Synechococcus*, grown in chemostat cultures, displays a markedly different pattern of isotopic fractionation compared to the eukaryotes studied (Popp et al., 1998; Figure S7). Although specific involvement of NDH in hydroxylation remains unknown for red-lineage phytoplankton such as diatoms and haptophytes, a functional homologue of this enzyme or the LCIB protein may be utilized. Our invoked hydroxylation step is similar to previously proposed roles for CAs (*e.g.*, the “chloroplast pump model”; Hopkinson, 2014), but with the important distinctions that it would be irreversible and would respond directly to photon flux.

Available genomic and physiological evidence indicates that the other CCM components invoked in our model—namely the association of the thylakoids with the pyrenoid, plus collocated CAs—have evolved multiple discrete times in phytoplankton. For example, new phytoplanktonic CAs, lacking sequence homology to known forms but with similar activities, are still being discovered (Kikutani et al., 2016; Jin et al., 2016; Hopkinson et al., 2016; Shen et al., 2017; Jensen et al., 2019). Yet, collectively, the

behavior of ε_p in cultures and in the marine record is surprisingly coherent, indicating that in most cases the similar physiological functions of these convergently-evolved CCMs reduce to a common set of isotopic consequences.

4.3 Physiological predictions of the model

Increases in photon flux correspond to an increase in the relative amount of the hydroxylation reaction (higher ω). This implies an increase in CO_2 availability at RubisCO compared to predictions based on passive diffusion alone (e.g., Rau et al., 1996). Physiologically, this implies that ε_p will get larger at a given $[\text{CO}_{2(\text{aq})}]$, due to greater expression of ε_{HYD} relative to $\varepsilon_{\text{RubisCO}}$. Such reasoning can explain the apparent conundrum that ε_p values in light-limited, nutrient-rich batch cultures of *E. huxleyi* become larger when growth rates are increased by lengthening the photoperiod or by increasing the light source intensity (Rost et al., 2002): the directional change in ε_p is an increase due to higher ω , while the concomitant, ω -induced increase in *internal* CO_2 supply also increases μ (and therefore $\mu/[\text{CO}_{2(\text{aq})}]$). In batch cultures of *P. tricornutum*, ε_p also appears to increase with increasing growth rates in response to a longer daylength or increased light intensity; however, the pattern is less pronounced (Riebesell et al., 2000). This taxonomic difference may be explained by the larger isotope effect associated with diatom RubisCO (18.5‰) compared to *E. huxleyi* (11‰): the diatom $\varepsilon_{\text{RubisCO}}$ value is closer to the ε_{HYD} endmember (25‰), making ω -induced changes in ε_p more difficult to resolve.

In chemostat cultures, growth rate is controlled by the delivery of nutrients, so excess light can be directed to hydroxylation to meet carbon demand at all growth rates. In the model, this is indexed as $\omega \approx 1$ (a constant), and the slow step of carbon acquisition is always predicted to have $\varepsilon_f = 25\text{‰}$. This means that ε_p always will decrease with increasing growth rates, consistent with measurements from chemostat cultures (Popp et al., 1998; Wilkes et al., 2017).

The model also predicts the relative fluxes of CO_2 and HCO_3^- across the cell membrane, which have been the focus of many studies of algal physiology (e.g., Colman et al., 2002, Tchernov et al., 2003,

Hoins et al., 2016b). For most of the taxa and culture conditions considered in this study, we find that HCO_3^- import is predicted to represent an increasing percentage of gross inorganic carbon uptake as $[\text{CO}_{2(\text{aq})}]$ declines (Figure S6). This uptake is sometimes accompanied by a net efflux of CO_2 from the cell, an outcome consistent with measurements using membrane-inlet mass spectrometry (MIMS) which can occasionally show a net efflux of CO_2 (Tchernov et al., 2003). Physiologically, a net efflux of CO_2 in our model implies that the ω pathway is recapturing and directly channeling imported carbon to RubisCO in the pyrenoid, rather than facilitating diffusive CO_2 entry at the cell boundary. This prediction about the ω pathway is consistent with a growing consensus in the literature asserting the importance of thylakoid-based CCMs for CO_2 recapture around RubisCO (Matsuda et al., 2017; Tsuji et al., 2017; Griffiths et al., 2017).

However, the model's prediction of net CO_2 efflux for some experimental conditions disagrees with a significant body of other MIMS measurements indicating a predominantly net influx of inorganic carbon into phytoplankton cells (e.g., Hopkinson et al., 2011; Hoins et al., 2016b). The disagreement between some of our model results (predicted net efflux) and these studies (predicted net influx) may indicate that our assumptions about fixed permeability coefficients or γ values across growth conditions are too rigid. If different membrane permeabilities or γ values are adopted for different taxa or growth conditions, our predictions for the significance of HCO_3^- import and CO_2 influx vs. efflux change. For example, increasing P_C from 0.0085 to 0.027 cm s^{-1} for *E. huxleyi* in chemostat cultures also produces an excellent model fit but requires a more prominent role for bicarbonate import and associated efflux of CO_2 , whereas decreasing P_C below 0.0085 would decrease bicarbonate import and promote CO_2 influx. Matsui et al. (2018) recently demonstrated that even in *P. tricornutum*, for which permeability coefficients have been measured, aquaporins can be expressed in a nitrogen- and CO_2 -dependent manner, altering the permeability of the cell to CO_2 . Moreover, Mangan et al. (2016) demonstrate that membrane permeabilities to HCO_3^- are likely dynamic, influenced by pH gradients across membranes. Thus, permeability measurements for more taxa acclimated to a wider range of growth conditions would help to clarify the best choices for these model

parameters and reconcile outstanding questions regarding the importance, energetic efficiency, and regulation of HCO_3^- import.

5. Conclusions: Implications for interpreting paleoenvironmental conditions

The experimentally determined relationship, $\varepsilon_{\text{p_maximum}} = \varepsilon_{\text{f}} \approx 25\text{‰}$, influences both the paleoenvironmental and the evolutionary conclusions drawn from paired organic and inorganic carbon isotope records. Estimates of ε_{p} for the Phanerozoic consistently do not exceed this value (Hayes et al., 1999; Witkowski et al., 2018), which has been argued to establish an upper limit of sensitivity of ε_{p} to changes in CO_2 concentrations that is ~ 8 - 10 times pre-industrial atmospheric levels, or ~ 2200 ppm CO_2 (e.g., Freeman, 2001; Freeman and Pagani, 2005; Pancost et al., 2013). Within this framework, any variability in sedimentary ε_{p} records would imply that $p\text{CO}_2$ is below 2200 ppm, regardless of the algal taxonomic source or nutrient environment (Freeman, 2001). Conversely, if temporal records of ε_{p} are approximately 25‰ and do not vary, this would argue that atmospheric $p\text{CO}_2$ is above the threshold of sensitivity.

The model presented here suggests another cause for variations in ε_{p} values, even under high $p\text{CO}_2$ atmospheres: a relative limitation of growth by photon flux. In this resource condition, ε_{p} values would still scale directly with $p\text{CO}_2$, but the maximum value of ε_{p} , even at the limit of very high CO_2 , would be influenced by the taxonomic identity of the phytoplankton contributing to carbon export and burial, as well as how and where they grow. This may help to reconcile apparent contradictions in the sedimentary record. For example, it may help to explain time intervals (e.g., the Cambrian through the Devonian, or the late Jurassic) when geochemical models predict $p\text{CO}_2$ exceeded 2200 ppm globally (Bernier and Kothavala, 2001), yet reconstructed ε_{p} values are $< 25\text{‰}$ and show variability (Hayes et al., 1999, Kuhn, 2007, Pagani, 2014, Witkowski et al., 2018). Variations in ε_{p} during these times might reflect enhanced nutrient availability coinciding with major ecological transitions, including the diversification and radiation of coccolithophores and dinoflagellates during the Jurassic (Wiggin et al., 2018). Alternatively, ε_{p} variability

might simply reflect changes in habitat depth within the photic zone and/or other physical factors affecting the rate of photon flux.

In the modern ocean, nutrient conditions influence ε_p values through associated changes in μ (Bidigare et al., 1997; Pagani, 2014). In our model, the distinction is that when nutrients are replete or light availability is low, the maximum expression of ε_p becomes dependent on $\varepsilon_{\text{RubisCO}}$, which has taxonomic variability. While accounting for both taxonomy and resource limitation certainly complicates interpretation of the sedimentary record, it also adds a dimension of predictive power with respect to prevailing growth conditions. For example, where ε_p records do reach a maximum of 25‰, this implies both high ambient CO_2 levels *and* a resource environment low in nutrients (*i.e.*, oligotrophy).

Field studies in the modern environment demonstrate these points. For example, our model suggests a revised explanation for why modern coastal diatoms growing in upwelling zones are relatively ^{13}C -enriched, even though $[\text{CO}_{2(\text{aq})}]$ is higher in upwelling zones compared to offshore regions or gyres (Pancost et al., 1997, Rau et al., 2001, Tolosa et al., 2008). Their values of ω may be near zero and ε_f may be approaching $\varepsilon_{\text{RubisCO}}$. The result would be greater ^{13}C enrichment regardless of the uncertain or variable extent of active HCO_3^- uptake (Fry and Wainright, 1991, Pancost et al., 1997; Tolosa et al., 2008; Hansman and Sessions, 2015). Conversely, to illustrate the nutrient-limited principle, modern haptophyte algae growing in oligotrophic waters produce ε_p values as large as $\sim 19\%$ (Laws et al., 2001; Tolosa et al., 2008; Pagani, 2014), clearly exceeding the 11‰ value of $\varepsilon_{\text{RubisCO}}$.

The best examples of ε_p approaching $\varepsilon_{\text{RubisCO}}$ may be the present-day Peru upwelling zone. Here, alkenone-based ε_p values from nitrate-replete waters correlate with $[\text{CO}_{2(\text{aq})}]$ and reach a maximum measured value of 11.2‰ under the highest CO_2 condition ($\sim 29 \mu\text{mol kg}^{-1}$; Bidigare et al., 1997; Pancost et al. 1997). This is in excellent agreement with the $\sim 11\%$ value of $\varepsilon_{\text{RubisCO}}$ for *E. huxleyi* (Boller et al., 2011), which would be predicted to be the dominant isotopic control as $\omega \rightarrow 0$ in this high nutrient flux setting. Simultaneously, diatom ε_p values (from diatom biomarkers; Pancost et al., 1997), exhibited ε_p values with a less well-defined relationship to CO_2 , but reaching a maximum value of 19.3‰. This agrees

with the *in vitro* isotope effect for diatom RubisCO (18.5‰). Nearly all of the diatom and alkenone-based ϵ_P measurements from this location are smaller than would be predicted using the classic $\epsilon_P = \epsilon_f - \mu / [\text{CO}_{2(\text{aq})}]$ equation applied to the ambient conditions (Laws et al., 1995; Pancost et al., 1997). Thus, the Peru upwelling results can be understood in terms of the influence of RubisCO on the expression of ϵ_P in these low- ω conditions.

Contrasting with the Peru data, alkenone-derived ϵ_P values from oligotrophic systems are large (~14–19‰), even though $[\text{CO}_{2(\text{aq})}]$ in these systems is lower than in the Peru upwelling zone (Bidigare et al., 1997; Tolosa et al., 2005). Our model predicts that this is due to a greater relative flux through the hydroxylation mechanism (higher ω), *i.e.*, ϵ_P is controlled primarily by ω and μ .

Overall, our generalized phytoplankton model can account for the important features of carbon isotope fractionation in red-lineage eukaryotic phytoplankton, both in cultures and in the environment. It incorporates CO_2 levels, algal physiology, and consensus observations from the literature regarding CCMs. The model performs better with accurate estimates of cellular surface area and volume, indicating that strategies for measuring these parameters from the geologic record and modern ocean are important. To this end, new approaches that involve analyzing organic matter bound to size-sorted fossilized components of phytoplankton (*e.g.*, the silica frustules of diatoms, the calcite liths of coccolithophores, or the organic cysts of dinoflagellates; Mejía et al., 2017; Sluijs et al. 2017; Wilkes et al., 2018) are being developed. However, our model introduces clear endmember predictions that are independent of these considerations in the limit as $\mu/\text{CO}_2 \rightarrow 0$, potentially providing information about multiple facets of past environments (CO_2 , growth conditions, and/or algal community composition). The model also provides a physiological explanation for why $p\text{CO}_2$ approaches appear to work in some contexts yet yield ambiguous results in others.

It also is essential to explore whether the isotopic patterns invoked here can be extended to green-lineage phytoplankton, picoeukaryotes, and other taxa that are not yet adequately represented by *in vivo* and *in vitro* carbon isotope studies. This will permit assessment of ϵ_P values earlier in Earth history. Our

model underscores the need to know the isotope effects associated with algal RubisCOs *in vitro*—both to test the hypothesis underpinning our model and to interpret the marine isotope record in high-nutrient environments. However, overall, the mechanisms for control of ε_p suggested here point to the central importance of understanding carbon uptake, transformation, and intracellular sequestration. These processes may respond directly to photosynthetic activity in aquatic organisms *via* links between the energetics of photosynthesis and the uptake of inorganic carbon.

Acknowledgements

This material is based upon work supported by the National Science Foundation Graduate Research Fellowship under Grant No. DGE1144152 to E.B.W. Any opinion, findings, and conclusions or recommendations expressed in this material are those of the authors and do not necessarily reflect the views of the National Science Foundation. Funding from the Agouron Institute (to E.B.W.) also supported this work. A.P. acknowledges funding from the Gordon and Betty Moore Foundation and NASA-NAI CAN6 (PI Roger Summons, MIT). We thank Pratigya Polissar, David Johnston, Boswell Wing, Itay Halevy, Alex Worden, and Rich Pancost for helpful discussions, John Kondziolka for assistance with Matlab script development, Sarah Feakins for editorial handling, and three anonymous reviewers for their valuable comments.

References

- Bach L. T., Mackinder L. C., Schulz K. G., Wheeler G., Schroeder D. C., Brownlee C., and Riebesell U. (2013) Dissecting the impact of CO₂ and pH on the mechanisms of photosynthesis and calcification in the coccolithophore *Emiliana huxleyi*. *New Phytol.* **199**, 121–134.
- Badger M. R., Andrews T. J., Whitney S. M., Ludwig M., Yellowlees D. C., Leggat W., and Price G. D. (1998) The diversity and coevolution of Rubisco, plastids, pyrenoids, and chloroplast-based CO₂-concentrating mechanisms in algae. *Can. J. Bot.* **76**, 1052–1071.
- Baullier B., Berne N., Murik O., Petroustos D., Prihoda J., Tanaka A., Villanova V., Bligny R., Flori S., Falconet D., KriegerLiszky A., Santabarbara S., Rappaport F., Joliot P., Tirichine L., Falkowski P. G., Cardol P., Bowler C., and Finazzi G. (2015) Energetic coupling between plastids and mitochondria drives CO₂ assimilation in diatoms. *Nature* **524**, 366–369.
- Beardall J., Griffiths H., and Raven J. A. (1982) Carbon isotope discrimination and the CO₂ accumulating mechanism in *Chlorella emersonii* (Chlorophyceae). *J. Phycol.* **17**, 134–141.
- Benthien A., Zondervan I., Engel A., Hefter J., Terbrüggen A., and Riebesell U. (2007) Carbon isotopic fractionation during a mesocosm bloom experiment dominated by *Emiliana huxleyi*: Effects of CO₂ concentration and primary production. *Geochim. Cosmochim. Ac.* **71**, 1528–1541.
- Berner R. and Kothavala Z. (2001) Geocarb III: A revised model of atmospheric CO₂ over Phanerozoic time. *Am. J. Sci.* **301**, 182–204.
- Bidigare R. R., Fluegge A., Freeman K. H., Hanson K. L., Hayes J. M., Hollander D., Jasper J. P., King L. L., Laws E. A., Milder J., Miller F. J., Pancost R., Popp B. N., Steinberg P. A., and Wakeham S. G. (1997) Consistent fractionation of ¹³C in nature and in the laboratory: Growth-rate effects in some haptophyte algae. *Global Biogeochem. Cy.* **11**, 279–292.
- Boller A. J., Thomas P. J., Cavanaugh C. M., and Scott K. M. (2011) Low stable carbon isotope fractionation by coccolithophore RubisCO. *Geochim. Cosmochim. Ac.* **75**, 7200–7207.
- Boller A. J., Thomas P. J., Cavanaugh C. M., and Scott K. M. (2015) Isotopic discrimination and kinetic parameters of RubisCO from the marine bloom-forming diatom, *Skeletonoma costatum*. *Geobiology* **13**, 33–43.
- Bolton C. T. and Stoll H. M. (2013) Late Miocene threshold response of marine algae to carbon dioxide limitation. *Nature* **500**, 558–562.
- Burkhardt S., Riebesell U., Zondervan I. (1999a) Effects of growth rate, CO₂ concentration, and cell size on the stable carbon isotope fractionation in marine phytoplankton. *Geochim. Cosmochim. Acta* **63**, 3729–3741.
- Burkhardt S., Riebesell U., Zondervan I. (1999b) Stable carbon isotope fractionation by marine phytoplankton in response to daylength, growth rate, and CO₂ availability. *Mar.Ecol. Prog. Ser.* **184**, 31–41.
- Burkhardt S., Amoroso G., Riebesell U., and Sültemeyer D. (2001) CO₂ and HCO₃ uptake in marine diatoms acclimated to different CO₂ concentrations. *Limnol. Oceanogr.* **46**, 1378–1391.
- Bundy H. F. (1986) Comparative kinetics and inhibition of a carbonic anhydrase from *Chlamydomonas reinhardtii*. *Comp. Biochem. Physiol.* **84B**, 63–69.

- Cassar N. (2003) Carbon-concentrating mechanisms and β -carboxylation: Their potential contribution to marine photosynthetic carbon isotope fractionation. Doctoral dissertation, University of Hawai'i.
- Cassar N., Laws E. A., and Popp B. N. (2006) Carbon isotopic fractionation by the marine diatom *Phaeodactylum tricornutum* under nutrient- and light-limited growth conditions. *Geochim. Cosmochim. Ac.* **70**, 5323–5335.
- Chrachri A., Hopkinson B. M., Flynn K., Brownlee C., and Wheeler G. L. (2018) Dynamic changes in carbonate chemistry in the microenvironment around single marine phytoplankton cells. *Nat. Commun.* **9**, 74.
- Clark I. D. and Lauriol B. (1992) Kinetic enrichment of stable isotopes in cryogenic calcites. *Chem. Geol.* **102**, 217–228.
- Colman B., Huertas E., Bhatti S., and Dason J. S. (2002) The diversity of inorganic carbon acquisition mechanisms in eukaryotic microalgae. *Funct. Plant Biol.* **29**, 261–270.
- Darienko T., Gustavs L., Eggert A., Wolf W., and Pröschold T. (2015) Evaluating the species boundaries of green microalgae (*Coccomyxa*, Trebouxiophyceae, Chlorophyta) using integrative taxonomy and DNA barcoding with further implications for the species identification in environmental samples. *PLoS One* **10**, e0127838.
- Davis, B. D. (1958) On the importance of being ionized. *Archives of Biochemistry and Biophysics* **78**, 497–508.
- Desmarais J. J., Flamholz A. I., Blikstad C., Dugan E. H., Laughlin T. G., Oltrogge L. M., Chen A. W., Wetmore K., Diamond S., Wang J. Y., and Savage D. F. (2019) DABs are inorganic carbon pumps found throughout prokaryotic phyla. *Nat. Microbiol.* 1–12.
- Eberlein T., Van de Waal D. B., and Rost B. (2014) Differential effects of ocean acidification on carbon acquisition in two bloom-forming dinoflagellate species. *Physiol. Plant.* **151**, 468–479.
- Eichner M., Thoms S., Kranz S. A., and Rost B. (2015) Cellular inorganic carbon fluxes in *Trichodesmium*: a combined approach using measurements and modelling. *J. Exp. Bot.* **66**, 749–759.
- Engel B. D., Schaffer M., Kuhn C., Villa L., Plitzko J. M., and Baumeister W. (2015) Native architecture of the *Chlamydomonas* chloroplast revealed by in situ cryo-electron tomography. *eLife* **4**, 304889.
- Farquhar G. D., O'Leary M. H., and Berry J. A. (1982) On the relationship between carbon isotope discrimination and the intercellular carbon dioxide concentration in leaves. *Aust. J. Plant Physiol.* **9**, 121–137.
- Farquhar G. D., Ehleringer J. R., and Hubick K. T. (1989) Carbon isotope discrimination and photosynthesis. *Annu. Rev. Plant. Phys.* **40**, 503–537.
- Francois R., Altabet M. A., Goericke R., McCorkle D. C., Brunet C., and Poisson A. (1993) Changes in the $\delta^{13}\text{C}$ of surface water particulate organic matter across the sub-tropical convergence in the S.W. Indian Ocean. *Global Biogeochem. Cycles* **7**, 627–644.
- Freeman K. H. (2001) Isotopic biogeochemistry of marine organic carbon. *Rev. Mineral. Geochem.* **43**, 579–605.

- Freeman K. H. and Pagani M. (2005) Alkenone-based estimates of past CO₂ levels: a consideration of their utility based on an analysis of uncertainties. In *A History of Atmospheric CO₂ and Its Effects on Plants, Animals, and Ecosystems* (eds. J. R. Ehleringer, T. E. Cerling, and M. D. Dearing). pp. 35–61. Springer, New York.
- Fridlyand L., Kaplan A., and Reinhold L. (1996) Quantitative evaluation of the role of a putative CO₂-scavenging entity in the cyanobacterial CO₂-concentrating mechanism. *Biosystems* **37**, 229–238.
- Fry B. and Wainwright S. C. (1991) Diatom sources of ¹³C-rich carbon in marine food webs. *Mar. Ecol. Prog. Ser.* **76**, 149–15.
- Goericke R., Montoya J., and Fry B. (1994) Physiology of isotopic fractionation in algae and cyanobacteria. In *Stable Isotopes in Ecology and Environmental Science* (eds. K. Lajtha and R. Michener). pp. 187–221. Blackwell Scientific Publications, Oxford.
- Griffiths H., Meyer M. T., and Rickaby R. E. M. (2017) Overcoming adversity through diversity: aquatic carbon concentrating mechanisms. *J. Exp. Bot.* **68**, 3689–3695.
- Guy R. D., Fogel M. L., and Berry J. A. (1993) Photosynthetic fractionation of the stable isotopes of oxygen and carbon. *Plant Physiol.* **101**, 37–47.
- Hansman R. L. and Sessions A. L. (2015) Measuring the *in situ* carbon isotopic composition of distinct marine plankton populations sorted by flow cytometry. *Limnol. Oceanogr-Meth.* **14**, 87–99.
- Hayes J. M. (2001) Fractionation of carbon and hydrogen isotopes in biosynthetic processes. *Rev. Mineral. Geochem.* **43**, 225–277.
- Hayes J. M., Strauss H., and Kaufman A. J. (1999) The abundance of ¹³C in marine organic matter and isotopic fractionation in the global biogeochemical cycle of carbon during the past 800 Ma. *Chem. Geol.* **161**, 103–125.
- Hennon, G. M. M., Ashworth, J., Groussman, R. D., Berthiaume, C., Morales, R. L., Baliga, N. S., et al. (2015). Diatom acclimation to elevated CO₂ via cAMP signalling and coordinated gene expression. *Nat. Clim. Chang.* **5**, 761–765. doi: 10.1038/nclimate2683
- Heureux, A. M. C., Young, J. N., Whitney S. M., Eason-Hubbard M. R., Lee R. B. Y., Sharwood, R. E., Rickaby, R. E. M. (2017) The role of Rubisco kinetics and pyrenoid morphology in shaping the CCM of haptophyte microalgae. *J. Exp. Bot.* **68**, 3959–3969.
- Höhner R., Aboukila A., Kunz, H-H., and Venema K. (2016) Proton gradients and proton-dependent transport processes in the chloroplast. *Front. Plant Sci.* **7**, 218.
- Hoins M., Van de Waal D. B., Eberlein T., Reichart G.-J., Rost B., and Sluijs A. (2015) Stable carbon isotope fractionation of organic cyst-forming dinoflagellates: Evaluating the potential for a CO₂ proxy. *Geochim. Cosmochim. Ac.* **160**, 267–276.
- Hoins M., Eberlein T., Großmann C. H., Brandenburg K., Reichart G.-J., Rost B., Sluijs, A., and Van de Waal, D. B. (2016a) Combined effects of ocean acidification and light or nitrogen availabilities on ¹³C fractionation in marine dinoflagellates. *PLoS ONE* **11**, e0154370.
- Hoins M., Eberlein T., Van de Waal D. B., Sluijs A., Reichart G.-J., and Rost B. (2016b) CO₂-dependent carbon isotope fractionation in dinoflagellates relates to their inorganic carbon fluxes. *J. Exp. Mar. Biol. Ecol.* **481**, 9–14.

- Holtz L-M., Wolf-Gladrow D., and Thoms S. (2017) Stable carbon isotope signals in particulate organic and inorganic carbon of coccolithophores – A numerical model study for *Emiliania huxleyi* **420**, *J. Theor. Biol.* 117–127.
- Hopkinson B. M., Dupont C. L., Allen A. E., Morel F. M. M. (2011) Efficiency of the CO₂-concentrating mechanism of diatoms. *Proceedings of the National Academy of Sciences USA* 108:3830–3837.
- Hopkinson B. M. (2014) A chloroplast pump model for the CO₂ concentrating mechanism in the diatom *Phaeodactylum tricornutum*. *Photosynth Res* **121**, 223–233.
- Hopkinson B. M., Dupont C. L., and Matsuda Y. (2016) The physiology and genetics of CO₂ concentrating mechanisms in model diatoms. *Curr. Opin. Plant Biol.* **31**, 51–57.
- Jasper J. P. and Hayes J. M. (1990) A carbon isotope record of CO₂ levels during the late Quaternary. *Nature* **347**, 462–464.
- Jensen E. L., Clement R., Kosta A., Maberly S. C., and Gontero B. (2019) A new widespread subclass of carbonic anhydrase in marine phytoplankton. *ISME J.* **13**, 2094–2106.
- Jin S., Sun J., Wunder T., Tang D., Cousins A. B., Sze S. K., Mueller-Cajar O., and Gao Y-G. (2016) Structural insights into the LCIB protein family reveals a new group of β -carbonic anhydrases. *Proc. Natl. Acad. Sci.* **113**, 14716–14721.
- Kaplan, A. and Reinhold, L. (1999) CO₂ concentrating mechanisms in photosynthetic microorganisms. *Annu. Rev. Plant Physiol. Plant Mol. Biol.* **50**, 539–570.
- Keller M. A., Piedrafita G., and Ralser M. (2015) The widespread role of non-enzymatic reactions in cellular metabolism. *Curr. Opin. Biotech.* **34**, 153–161.
- Kikutani, S., Tanaka, R., Yamazaki, Y., Hara, S., Hisabori, T., Kroth, P.G., and Matsuda, Y. (2012) Redox regulation of carbonic anhydrases via thioredoxin in chloroplast of the marine diatom *Phaeodactylum tricornutum*. *J. Biol. Chem.* **287**, 20689–20700.
- Kikutani S., Nakajima K., Nagasato C., Tsuji Y., Miyatake A., and Matsuda Y. (2016) Thylakoid luminal θ -carbonic anhydrase critical for growth and photosynthesis in the marine diatom *Phaeodactylum tricornutum* *Proc. Nat. Acad. Sci.* **113**, 9828–9833.
- Kranz S. A., Young J. N., Hopkinson B. M., Goldman J. A. L., Tortell P. D., and Morel F. M. M. (2015) Low temperature reduces the energetic requirement for the CO₂ concentrating mechanism in diatoms. *New Phytologist* **205**, 192–201.
- Kuhn T. (2007) The evolution of the photosynthetic carbon isotope fractionation ϵ_p of marine phytoplankton during the Devonian to Permian time interval Ph.D. diss., University Erlangen-Nuremberg.
- Laws E. A., Popp B. N., Bidigare R. R., Kennicutt M. C., and Macko S.A. (1995) Dependence of phytoplankton carbon isotopic composition on growth rate and CO_{2aq}: Theoretical considerations and experimental results. *Geochim. Cosmochim. Ac.* **59**, 1131–1138.
- Laws E. A., Bidigare R. R., and Popp B. N. (1997) Effect of growth rate and CO₂ concentration on carbon isotope fractionation by the marine diatom *Phaeodactylum tricornutum*. *Limnol. Oceanogr.*, **42**, 1552–1560.

- Laws E. A., Popp B. N., Bidigare R. R., Riebesell U., Burkhardt S., and Wakeham S. G. (2001) Controls on the molecular distribution and carbon isotopic composition of alkenones in certain haptophyte algae. *Geochem. Geophys. Geosyst.* **2**, 2000GC000057.
- Laws E. A., Popp B. N., Cassar N., and Tanimoto J. (2002) ^{13}C discrimination patterns in oceanic phytoplankton: likely influence of CO_2 concentrating mechanisms, and implications for palaeoreconstructions. *Funct. Plant Biol.* **29**, 323-333.
- Maeda S., Badger M. R., and Price G. D. (2002) Novel gene products associated with NdhD3/D4-containing NDH-1 complexes are involved in photosynthetic CO_2 hydration in the cyanobacterium *Synechococcus* sp. PCC7942. **43**, 425–435.
- Mangan N. M., Flamholz A., Hood R. D., Milo R., and Savage D. F. (2016) pH determines the energetic efficiency of the cyanobacterial CO_2 concentrating mechanism. *Proc. Nat. Acad. Sci.* **113**, E5354–E5362.
- Marlier J. F. and O’Leary M. H. (1984) Carbon kinetic isotope effects on the hydration of carbon dioxide and the dehydration of bicarbonate ion. *J. Am. Chem. Soc.* **106**, 5054-5057.
- Matsuda Y., Nakajima K., and Tachibana M. (2011) Recent progresses on the genetic basis of the regulation of CO_2 acquisition systems in response to CO_2 concentration. *Photosynth. Res.* **109**, 191–203.
- Matsuda Y., Hopkinson B. M., Nakajima K., Dupont C. L., and Tsuji Y. (2017) Mechanisms of carbon dioxide acquisition and CO_2 sensing in marine diatoms: a gateway to carbon metabolism. *Philos. Trans. R. Soc. Lond. B.* **372**, 20160403.
- Matsui H., Hopkinson B. M., Nakajima K., and Matsuda Y. (2018) Plasma membrane-type aquaporins from marine diatoms function as CO_2/NH_3 channels and provide photoprotection. *Plant Physiol.* **178**, 345–357.
- McClelland H. L. O., Bruggeman J., Hermoso M, and Rickaby R. E. M. (2017) The origin of carbon isotope vital effects in coccolith calcite. *Nat. Commun.* **8**, 14511.
- McNevin D. B., Badger M. R., Kane H. J., and Farquhar G. D. (2006) Measurement of (carbon) kinetic isotope effect by Rayleigh fractionation using membrane inlet mass spectrometry for CO_2 -consuming reactions. *Funct. Plant Biol.* **33**, 1115–1128.
- McNevin D. B., Badger M. R., Whitney S. M., von Caemmerer S., Tcherkez G. G. B., and Farquhar G. D. (2007) Differences in carbon isotope discrimination of three variants of D-Ribulose-1,5-bisphosphate Carboxylase/Oxygenase reflect differences in their catalytic mechanisms. *J. Biol. Chem.* **282**, 36068–36076.
- Mejía M., Méndez-Vicente A., Abrevaya L., Lawrence K. T., Ladlow C., Bolton C., Cacho I., and Stoll H. (2017) A diatom record of CO_2 decline since the late Miocene. *Earth and Planetary Science Letters* **479**, 18–33.
- Meyer M. T., Whittaker C., Griffiths H. (2017) The algal pyrenoid: key unanswered questions. *J. Exp. Bot.* **68**, 3739–3749.
- Mitchell M.C., Meyer M.T., and Griffiths, H. (2014) Dynamics of carbon concentrating mechanism induction and protein relocalization during the dark-to-light transition in synchronized *Chlamydomonas reinhardtii*. *Plant Physiol.* **166**, 1073–1082.

- Mitchell M. C., Metodieva G., Metodiev M. V., Griffiths H. and Meyer M. T. (2017) Pyrenoid loss impairs carbon-concentrating mechanism induction and alters primary metabolism in *Chlamydomonas reinhardtii* **68**, 3891–3902.
- Montagnes D.J.S., Berges J.A., Harrison P.J., and Taylor F.J.R. (1994) Estimating carbon, nitrogen, protein, and chlorophyll *a* from volume in marine phytoplankton. *Limnol. Oceanogr.* **39**, 1044–1060.
- Moroney J. V. and Ynalvez R. A. (2007) Proposed carbon dioxide concentrating mechanism in *Chlamydomonas reinhardtii*. *Eukaryot. Cell* **6**, 1251–1259.
- Morse D., Salois P., Markovic P., and Hastings J. W. (1995) A nuclear-encoded form II RuBisCO in dinoflagellates. *Science* **268**, 1622–1624.
- Ogawa T. (1992) Identification and characterization of the *ictA/ndhL* gene product essential to inorganic carbon transport of *Synechocystis* PCC 6803. *Plant Physiol.* **99**, 1604–1608.
- Ogawa T. and Mi H. (2007) Cyanobacterial NADPH dehydrogenase complexes. *Photosynth. Res.* **93**, 69–77.
- Ohkawa H., Sonoda M., Shibata M., and Ogawa T. (2001) Localization of NAD(P)H dehydrogenase in the cyanobacterium *Synechocystis* sp. Strain PCC 6803. *J. Bacteriol.* **183**, 4938–4939.
- O’Leary M. H. (1984) Measurement of the isotope fractionation associated with diffusion of carbon dioxide in aqueous solution. *J. Phys. Chem.* **88**, 823–825.
- O’Leary M. H., Madhavan S., and Paneth P. (1992) Physical and chemical basis of carbon isotope fractionation in plants. *Plant, Cell Environ.* **15**, 1099–1104.
- Pagani M. (2014) Biomarker-based inferences of past climate: The alkenone $p\text{CO}_2$ Proxy. In *Treatise on Geochemistry 2nd Ed.* (eds. H. Holland and K. Turekian). pp. 361–378, Elsevier, Amsterdam.
- Pagani M., Huber M. Liu Z., Bohaty S. M., Henderiks J., Sijp W., Krishnan S., and DeConto R. M. (2011) The role of carbon dioxide during the onset of Antarctic glaciation. *Science* **334**, 1261–1264.
- Pancost R. D., Freeman K. H., Wakeham S. G., and Robertson C. Y. (1997) Controls on carbon isotope fractionation by diatoms in the Peru upwelling region. *Geochim. Cosmochim. Ac.* **61**, 4983–4991.
- Pancost R. D., Freeman K. H., Herrmann A. D., Patzkowsky M. E., Ainsaar L., and Martma T. (2013) Reconstructing Late Ordovician carbon cycle variations. *Geochim. Cosmochim. Ac.* **105**, 433–454.
- Planq J., Grossi V., Henderiks J., Simon L., and Mattioli E. (2012) Alkenone producers during late Oligocene-early Miocene revisited. *Paleoceanography* **27**, PA 1202.
- Popp B. N., Laws E. A., Bidigare R. R., Dore J. E., Hanson K. L., and Wakeham S.G. (1998a) Effect of phytoplankton cell geometry on carbon isotopic fractionation. *Geochim. Cosmochim. Ac.* **62**, 69–77.
- Price G. D., Maeda S., Omata T., and Badger M. R. (2002) Modes of active carbon uptake in the cyanobacterium, *Synechococcus* sp. PCC7942. *Funct. Plant Biol.* **29**, 131–149.
- Pronina N. A and Borodin V. V. (1993) CO_2 stress and CO_2 concentration mechanism: investigation by means of photosystem-deficient and carbonic anhydrase-deficient mutants of *Chlamydomonas reinhardtii*. *Photosynthetica* **28**, 515–522.

- Ratti S., Giordano M., and Morse D. (2007) CO₂-concentrating mechanisms of the potentially toxic dinoflagellate *Protoceratium reticulatum* (Dinophyceae, Gonyaulacales). *J. Phycol.* **43**, 693–701.
- Rau G. H., Chavez F. P., and Friederich G. E. (2001) Plankton ¹³C/¹²C variations in Monterey Bay, California: evidence of non-diffusive inorganic carbon uptake by phytoplankton in an upwelling environment. *Deep-Sea Res. I* **48**, 79–94.
- Raven JA (1997) CO₂-concentrating mechanisms: A direct role for thylakoid lumen acidification? *Plant Cell Environ* 20(2):147–154.
- Raven J.A., Beardall J., and Giordano M. (2014) Energy costs of carbon dioxide concentrating mechanisms in aquatic organisms. *Photosynth. Res.* **121**, 111–124.
- Raven J. A. and Beardall J. (2015) The ins and outs of CO₂. *J. Exp. Bot.* **67**, 1–13.
- Rau G. H., Takahashi T., Des Marais D. J., Repeta D. J., and Martin J.H. (1992) The relationship between δ¹³C of organic matter and [CO_{2(aq)}] in ocean surface water: Data from a JGOFS site in the northeast Atlantic Ocean and a model. *Geochim. Cosmochim. Ac.* **56**, 1413–1419.
- Rau G.H., Riebesell U. and Wolf-Gladrow D. (1996) A model of photosynthetic ¹³C fractionation by marine phytoplankton based on diffusive molecular CO₂ uptake. *Mar. Ecol. Prog. Ser.* **133**, 275–285.
- Reinfelder J. R. (2011) Carbon concentrating mechanisms in eukaryotic marine phytoplankton. *Annu. Rev. Mar. Sci.* **3**, 291–315.
- Rickaby R. E. M., Heureux A. M. C., Eason Hubbard M. R., Chan I., McClelland H. L.O, Young J. N., Lee R. B. Y. and Hermoso M. (2015) Everything is not spinach: A history of evolving carbon affinity and isotopic fractionation in marine algal Rubisco. *Goldschmidt Abstracts* 2634.
- Riebesell U., Burkhardt S., Dauelsberg A., and Kroon B. (2000a) Carbon isotope fractionation by a marine diatom: Dependence on the growth-rate-limiting resource. *Mar. Ecol. Prog. Ser.* **193**, 295–303.
- Riebesell U., Revill, A. T., Holdsworth, D. G., and Volkman, J. K. (2000b) The effects of varying CO₂ concentration on lipid composition and carbon isotope fractionation in *Emiliania huxleyi*. *Geochim. Cosmochim. Ac.* **64**, 4179–4192.
- Robinson J. J., Scott K. M., Swanson S. T., O’Leary M. H., Horken K., Tabita F. R., and Cavanaugh C. M. (2003) Kinetic isotope effect and characterization of form II RubisCO from the chemoautotrophic endosymbionts of the hydrothermal vent tubeworm *Riftia pachyptila*. *Limnol. Oceanogr.* **48**, 48–54.
- Roeske C. and O’Leary M. H. (1984) Carbon isotope effects on enzyme-catalyzed carboxylation of ribulose biphosphate. *Biochemistry* **23**, 6275–6284.
- Roeske C. and O’Leary M. H. (1985) Carbon isotope effect on carboxylation of ribulose biphosphate catalyzed by ribulosebiphosphate carboxylase from *Rhodospirillum rubrum*. *Biochemistry-US* **24**,1603–1607.
- Rost B., Zondervan I., and Riebesell U. (2002) Light-dependent carbon isotope fractionation in the coccolithophorid *Emiliania huxleyi*. *Limnol. Oceanogr.* **47**, 120–128.
- Rost B., Riebesell U., and Burkhardt S. (2003) Carbon acquisition of bloom-forming marine phytoplankton. *Limnol. Oceanogr.* **48**, 55–67.

- Rowan R., Whitney S. M., Fowler A., and Yellowlees D. (1996) Rubisco in marine symbiotic dinoflagellates: form II enzymes in eukaryotic oxygenic phototrophs encoded by a nuclear multigene family. *Plant Cell* **8**, 539–553.
- Rost B., Riebesell U., Sültemeyer D. (2006) Carbon acquisition of marine phytoplankton: Effect of photoperiod length. *Limnol. Oceanogr.* **51**, 12–20.
- Sade Z. and Halevy I. (2017) New constraints on kinetic isotope effects during CO_{2(aq)} hydration and hydroxylation: Revisiting theoretical and experimental data. *Geochim. Cosmochim. Ac.* **214**, 246–265.
- Satoh D., Hiraoka Y., Colman B., and Matsuda Y. (2001) Physiological and molecular biological characterization of intracellular carbonic anhydrase from the marine diatom *Phaeodactylum tricornutum*. *Plant Physiol.* **126**, 1459–1470.
- Schulz K. G., Riebesell U., Rost B., Thoms S., and Zeebe R. E. (2006) Determination of the rate constants for the carbon dioxide to bicarbonate inter-conversion in pH-buffered seawater systems. *Marine Chemistry* **100**, 53–65.
- Schulz K. G., Rost B., Burkhardt S., Riebesell U., Thoms S., Wolf-Gladrow D. A. (2007) The effect of iron availability on the regulation of carbon acquisition in the coccolithophore *Emiliania huxleyi* and the significance of cellular compartmentation for stable carbon isotope fractionation. *Geochim. Cosmochim. Ac.* **71**, 5301–5312.
- Scott K. M., Schwedock J., Schrag D. P., and Cavanaugh C. M. (2004) Influence of form IA RubisCO and environmental dissolved inorganic carbon on the $\delta^{13}\text{C}$ of the chlam-chemoautotroph symbiosis *Solemya velum*. *Environ. Microbiol.* **6**, 1210–1219.
- Scott K. M., Henn-Sax M., Harmer T. L., Longo D. L., Frame C. H., and Cavanaugh C. M. (2007) Kinetic isotope effect and biochemical characterization of form IA RubisCO from the marine cyanobacterium *Prochlorococcus marinus* MIT9313. *Limnol. Oceanogr.* **52**, 2199–2204.
- Sharkey T. D. and Berry J. A. (1985) Carbon isotope fractionation of algae as influenced by an inducible CO₂ concentrating mechanism. In *Inorganic Carbon Uptake by Aquatic Photosynthetic Organisms* (eds. W. J. Lucas and J. A. Berry). pp. 389–401.
- Shen C., Dupont C. L., and Hopkinson B. M. (2017) The diversity of CO₂-concentrating mechanisms in marine diatoms as inferred from their genetic content. **68**, 3937–3948.
- Siegenthaler U. and Münich K. O. (1981) ¹³C/¹²C fractionation during CO₂ transfer from air to sea. In *Carbon Cycle Modelling* (ed. B. Bolin), Wiley, New York, 249–257.
- Sinetova, M.A., Kupriyanova, E., Markelova, A.G., Allakheverdiev, S.I., Pronina, N.A. (2012) Identification and functional role of the carbonic anhydrase Cah3 in thylakoid membranes of pyrenoid of *Chlamydomonas reinhardtii*. *Biochim. Biophys. Ac.* **1817**, 1248–1255.
- Sluijs A., Roij L., Frieling J., Laks I., and Reichart G.-J. (2017) Single-species dinoflagellate cyst carbon isotope ecology across the Paleocene-Eocene Thermal Maximum. *Geology* **46**, 79–82.
- Stoll H. M., Guitian J., Hernandez-Almeida I., Mejia L. M., Phelps S., Polissar P., Rosenthal Y., Zhang H., and Ziveri P. (2019) Upregulation of phytoplankton carbon concentrating mechanisms during low CO₂ glacial periods and implications for the phytoplankton pCO₂ proxy. *Quat. Sci.Rev.* **208**, 1–20.

- Tabita F. R., Satagopan S., Hanson T. E., Kreef N. E., and Scott S. S. (2008) Distinct form I, II, III, and IV Rubisco proteins from the three kingdoms of life provide clues about Rubisco evolution and structure/function relationships. *J. Exp. Bot.* **59**, 1515–1524.
- Tachibana M., Allen A. E., Kikutani S., Endo Y., Bowler C., Matsuda Y. (2011) Localization of putative carbonic anhydrases in two marine diatoms, *Phaeodactylum tricoratum* and *Thalassiosira pseudonana*. *Photosynth. Res.* **109**, 205–221.
- Tanaka Y., Nakatsuma D., Harada H., Ishida M., and Matsuda Y. (2005) Localization of soluble beta-carbonic anhydrase in the marine diatom *Phaeodactylum tricoratum*. Sorting to the chloroplast and cluster formation on the girdle lamellae. *Plant Physiol.* **138**, 207–217.
- Tanaka A., Ohno N., Nakajima K., and Matsuda Y. (2015) Light and CO₂/cAMP signal crosstalk on the promoter elements of chloroplastic β -carbonic anhydrase genes in the marine diatom *Phaeodactylum tricoratum*. *Plant Physiol.* **170**, 1105–1116.
- Tchernov D., Hassidim M., Luz B., Sukenik A., Reinhold L., and Kaplan A. (1997) Sustained net CO₂ evolution during photosynthesis by marine microorganism. *Curr. Biol.* **7**, 723–728.
- Tchernov D., Helman Y., Keren N., Luz B., Ohad I., Reinhold L., Ogawa T., and Kaplan A. (2001) Passive entry of CO₂ and its energy-dependent intracellular conversion to HCO₃⁻ in cyanobacteria are driven by a photosystem I-generated $\Delta\mu\text{H}^+$. *J. Biol. Chem.* **276**, 23450–23455.
- Tchernov D., Silverman J., Reinhold L. B., and Kaplan A. (2003) Massive light-dependent cycling of inorganic carbon between oxygenic photosynthetic microorganisms and their surroundings. *Photosynth. Res.* **77**, 95–103.
- Tchernov D. and Lipschultz F. (2008) Carbon isotopic composition of *Trichodesmium* spp. Colonies off Bermuda: effects of colony mass and season. *J. Plankton Res.* **30**, 21–31.
- Tcherkez G. G. B., Farquhar G. D., Andrews T. J. (2006) Despite slow catalysis and confused substrate specificity, all ribulose biphosphate carboxylases may be nearly perfectly optimized. *P. Natl. Acad. Sci. USA* **103**, 7246–7251.
- Thoms S., Pahlow M., and Wolf-Gladrow D. A. (2001) Model of the carbon concentrating mechanism in chloroplasts of eukaryotic algae. *J. theor. Biol.* **208**, 295–313.
- Tolosa I., Miquel J.-C., Gasser B., Raimbault P., Goyet C., and Claustre H. (2008) Distribution of lipid biomarkers and carbon isotope fractionation in contrasting trophic environments of the South East Pacific. *Biogeosciences* **5**, 949–968.
- Uzdowski E., Menschel G., and Hoefs J. (1982) Kinetically controlled partitioning and isotopic equilibrium of ¹³C and ¹²C in the system CO₂-NH₃-H₂O. *Z. Phys. Chem.* **130**, 13–21.
- Volokita M., Zenvirth D., Kaplan A., and Reinhold L. (1984) Nature of the inorganic carbon species actively taken up by the cyanobacterium *Anabaena variabilis*. *Plant Physiol.* **76**, 599–602.
- Wang Y., and Spalding M. H. (2014) Acclimation to very low CO₂: contribution of limiting CO₂ inducible proteins, LCIB and LCIA, to inorganic carbon uptake in *Chlamydomonas reinhardtii*. **166**, 2040–2050.
- Whitney S. M. and Andrews T. J. (1998) The CO₂/O₂ specificity of single-subunit ribulose-biphosphate carboxylase from the dinoflagellate, *Amphidinium carterae*, *Aust. J. Plant Physiol.* **25**, 131–138.

- Whitney S. M., Houtz R. L., and Alonso H. (2011) Advancing our understanding and capacity to engineer nature's CO₂-sequestering enzyme, Rubisco. *Plant Physiol.* **155**, 27–35.
- Whitney S. M., Shaw D. C., and Yellowlees D. (1995) Evidence that some dinoflagellates contain a ribulose-1,5-bisphosphate carboxylase/oxygenase related to that of the alpha-proteobacteria. *Proc. Biol. Sci.* **1356**, 271–275.
- Wiggan NJ, Riding JB, Fensome RA, Mattioli E. (2018) The Bajocian (Middle Jurassic): A key interval in the early Mesozoic phytoplankton radiation. *Earth Sci. Rev.* doi:10.1016/j.earscirev.2018.03.009.
- Wilkes E. B., Carter S. J., and Pearson A. (2017) CO₂-dependent carbon isotope fractionation in the dinoflagellate *Alexandrium tamarense*. *Geochim. Cosmochim. Ac.*, **212**, 48–61.
- Wilkes E. B., McClelland H. L. O., Rickaby R. E. M., and Pearson A. (2018) Carbon isotope ratios of coccolith-associated polysaccharides of *Emiliania huxleyi* as a function of growth rate and CO₂ concentration. *Org. Geochem.* **119**, 1–10.
- Witkowski C. R., Weijers J. W. H., Blais B., Schouten S., and Damsté J. S. S. (2018) Molecular fossils from phytoplankton reveal secular P_{CO_2} trend over the Phanerozoic. *Science Advances* **4**, 4556.
- Wong, W. W., Benedict, C. R., and Kohel, R. J. (1979) Enzymic fractionation of the stable carbon isotopes of carbon dioxide by Ribulose-1,5-bisphosphate Carboxylase *Plant Physiol.* **63**, 852–856.
- Yamano T., Tsujikawa T., Hatano K., Ozawa S., Takahashi Y., and Fukuzawa H. (2010) Light and low-CO₂-dependent LCIB-LCIC complex localization in the chloroplast supports the carbon-concentrating mechanism in *Chlamydomonas reinhardtii*. *Plant Cell Physiol.* **51**, 1453–1468.
- Young J. N., Heureux A. M. C., Sharwood R. E., Rickaby R. E. M., Morel F. M. M., and Whitney S. M. (2016) Large variation in the Rubisco kinetics of diatoms reveals diversity among their carbon-concentrating mechanisms. *J. Exp. Bot.* **67**, 3445-3456.
- Young J. N. and Hopkinson B.M. (2017) The potential for co-evolution of CO₂-concentrating mechanisms and Rubisco in diatoms. *J. Exp. Bot.* **68**, 3751-3762.
- Zeebe R. E. (2014) Kinetic fractionation of carbon and oxygen isotopes during hydration of carbon dioxide. *Geochim. Cosmochim. Ac.* **2014**, 540-552.
- Zeebe R. E. and Wolf-Gladrow, D. (2001) *CO₂ in Seawater: Equilibrium, Kinetics, Isotopes*. Elsevier Oceanography Series, Amsterdam.
- Zhang P., Battchikova N., Jansen T., Appel J., Ogawa T., and Aro E. M. (2004) Expression and functional roles of the two distinct NDH-1 complexes and the carbon acquisition complex NdhD3/NdhF3/CupA/SII1735 in *Synechocystis* sp. PCC 6803.

Tables & Figures

Table 1. Compiled $\epsilon_{\text{RubisCO}}$ and ϵ_f values for different RubisCO forms.

RubisCO Form	Biological Source	Organism Type	$\epsilon_{\text{RubisCO}}$ (‰) (<i>in vitro</i>)	Reference	ϵ_f (‰) (<i>in vivo</i>)	Reference
IA	<i>Solemya velum</i> symbiont	γ -Proteobacterium	24.5	Scott <i>et al.</i> (2004)	–	
	<i>Prochlorococcus marinus</i> MIT9313	Cyanobacterium	24	Scott <i>et al.</i> (2007)	–	
	<i>Synechococcus sp.</i>	Cyanobacterium	–	–	17	Popp <i>et al.</i> (1998)
IB	<i>Spinacia oleracea</i>	Higher Plant	26–30	Roeske & O’Leary (1984); Guy <i>et al.</i> (1993); Scott <i>et al.</i> (2004); McNevin <i>et al.</i> (2006)	–	
	<i>Gossypium</i>	Higher Plant	27.1	Wong <i>et al.</i> (1979)	–	
	<i>Nicotiana tabacum</i>	Higher Plant	27.4	McNevin <i>et al.</i> (2007)	–	
	<i>Synechococcus</i> PCC 6301 ^a	Cyanobacterium	21–22	Guy <i>et al.</i> (1993); McNevin <i>et al.</i> (2007)	–	
ID	<i>Emiliana huxleyi</i>	Coccolithophore	11.1	Boller <i>et al.</i> (2011)	25	Bidigare <i>et al.</i> (1997)
	<i>Skeletonema costatum</i>	Diatom	18.5	Boller <i>et al.</i> (2015)	–	
	<i>Phaeodactylum tricorutum</i>	Diatom	–	–	25	Laws <i>et al.</i> (1997)
	<i>Porosira glacialis</i>	Diatom	–	–	25	Popp <i>et al.</i> (1998)
II	<i>Riftia pachyptila</i> symbiont	γ -Proteobacterium	19.5	Robinson <i>et al.</i> (2003)	–	
	<i>Rhodospirillum rubrum</i>	α -Proteobacterium	18–23	Roeske & O’Leary (1985); Guy <i>et al.</i> (1993); McNevin <i>et al.</i> (2007)	–	
	<i>Alexandrium tamarense</i>	Peridinin-containing Dinoflagellate	–	–	27	Wilkes <i>et al.</i> (2017)

^a Freshwater cyanobacterium. PCC 6301 is a strain synonym for *Anacystis nidulans* and *Synechococcus* PCC 6301.

Figure Captions

Figure 1. Comparison of $\epsilon_{\text{RubisCO}}$ values measured *in vitro* with ϵ_f values determined *in vivo*. The data show the $\sim 25\%$ intercept (ϵ_f values) that result from plotting ϵ_p as a function of $\mu/[\text{CO}_{2(\text{aq})}]$ for eukaryotic phytoplankton grown in nitrate-limited chemostats. Lines represent geometric mean regression analysis. Black squares indicate the diatom *Phaeodactylum tricornutum* (Form ID RubisCO; Laws et al., 1997); dark grey triangles, calcifying and non-calcifying clones of the coccolithophore *Emiliania huxleyi* (Form ID RubisCO; Bidigare et al., 1997); light grey circles, dinoflagellate *Alexandrium tamarense* (Form II RubisCO; Wilkes et al., 2017); white diamonds, diatom *Porosira glacialis* (Form ID RubisCO; Popp et al., 1998). Ranges of $\epsilon_{\text{RubisCO}}$ measured *in vitro* (purified enzyme) are shown on the left side of the figure for RubisCO forms IA, IB, ID, and II (data, Table 1), with boxes shaded to correspond to the most similar chemostat-grown species.

Figure 2. Model structure. Dashed arrows indicate passive (diffusive) fluxes, thick solid arrows indicate either active transport processes or enzymatic conversions, and thin solid arrows indicate uncatalyzed chemical conversions. The invoked enzymes are RubisCO, carbonic anhydrase (CA), and a putative enzyme or other non-enzymatic process catalyzing the active hydroxylation of CO_2 to HCO_3^- (HYD). The interaction of photons with the thylakoid membrane is shown with a jagged arrow near the process of hydroxylation.

Figure 3. Net fluxes and isotopic compositions as a function of ω . (a-e) Carbon fluxes for a generic algal cell for the five (μ/CO_2) conditions highlighted in blue in Figure S3; C = CO_2 ; H = HCO_3^- . The cell is assumed to have an $\epsilon_{\text{RubisCO}}$ value of 11%. The parameter γ , governing active bicarbonate uptake, is uniformly assigned a value of 1.5 (except for case (c), in which $\gamma = 10$). The arrow widths and directions are scaled to represent net fluxes, with wider arrows corresponding to larger fluxes. Dotted grey arrows are used to represent non-zero fluxes that are several orders of magnitude smaller than the thinnest black

arrows. The relative isotopic compositions and CO₂ concentrations of the carbon pools are illustrated with the shading of each carbon pool or cellular compartment: darker blue corresponds to a higher degree of ¹³C enrichment and darker grey corresponds to a higher [CO_{2(aq)}]. Interconversion of CO₂ and HCO₃⁻ by CA is bidirectional; here the unidirectional arrows (*e.g.*, H_c→C_c) show only the net, not gross, fluxes. Gross fluxes are depicted in a corresponding supplementary figure, S4. **(f)** ϵ_p vs. μ/CO_2 outcomes for cases **a-e**.

Figure 4. Behavior of the generalized model for *A. tamarensis* (a, b, c) and *E. huxleyi* (d, e, f). Panels show the model sensitivity to parameters ω , γ , P_C , P_H , and empirical inputs representative of each taxon. The dinoflagellate *A. tamarensis* was modeled with $\epsilon_{\text{RubisCO}} = 19.5\%$, $SA = 4300 \mu\text{m}^2$, $V = 26500 \mu\text{m}^3$, $\text{POC} = 3500 \text{ pg C cell}^{-1}$, and default membrane permeability coefficients of $P_C = 2.70 \times 10^{-2} \text{ cm s}^{-1}$ and $P_H = 1.4 \times 10^{-5} \text{ cm s}^{-1}$; [CO_{2(aq)}] was varied from 0.25 to 150 $\mu\text{mol kg}^{-1}$ and μ_i was uniformly assumed to equal 0.1 d⁻¹. The coccolithophore *E. huxleyi* was modeled with $\epsilon_{\text{RubisCO}} = 11.1\%$, $SA = 88 \mu\text{m}^2$, $V = 77 \mu\text{m}^3$, $\text{POC} = 8.3 \text{ pg C cell}^{-1}$, and default membrane permeability coefficients of $P_C = 0.85 \times 10^{-2} \text{ cm s}^{-1}$ and $P_H = 1.4 \times 10^{-5} \text{ cm s}^{-1}$; [CO_{2(aq)}] was varied from 0.5 to 100 $\mu\text{mol kg}^{-1}$ and μ_i was uniformly assumed to equal 0.4 d⁻¹. **(a, d)** Influence of the parameter γ , controlling the flux of actively imported HCO₃⁻: high $\gamma = 4.5$ (solid lines) for both taxa vs. low $\gamma = 3$ for *A. tamarensis* and 1.8 for *E. huxleyi* (dashed lines). **(b, e)** All cell and culture parameters are identical to (a, d), except γ is held constant at the taxon-specific “low” value and membrane permeabilities to CO₂ are varied: high $P_C = 2.70 \times 10^{-2} \text{ cm s}^{-1}$ (solid lines) or low $P_C = 0.85 \times 10^{-2} \text{ cm s}^{-1}$ (dashed lines). **(c, f)** All cell and culture parameters are identical to (b, e), except membrane permeabilities to HCO₃⁻ are varied: high $P_H = 1.4 \times 10^{-5} \text{ cm s}^{-1}$ (solid lines) or low (default; Table S1) $P_H = 1.4 \times 10^{-6} \text{ cm s}^{-1}$ (dashed lines).

Figure 5. Modeled vs. measured ϵ_p values for the diatom *P. tricornutum*. **(a)** Measured ϵ_p values from nitrate and phosphate-limited chemostat cultures (Cassar, 2003; Laws et al., 1997) **(b)** Modeled ϵ_p values,

with $\gamma = 3.8$ and $\omega = 1.0$. **(c)** Comparison of modeled vs. measured ε_p values from (a) and (b). **(d)** Measured ε_p values from nutrient-replete batch cultures (Riebesell et al., 2000a; Burkhardt et al., 2000a,b). **(e)** Modeled ε_p values with $\gamma = 5.0$ and $\omega = 0.04 - 0.89$ (listed in the legend). **(f)** Comparison of modeled vs. measured ε_p values for (d) and (e). The horizontal dashed lines correspond to $\varepsilon_{\text{RubisCO}} = 18.5\text{‰}$ (*in vitro*; Table 1). Results are detailed in TableS9.

Figure 6. Modeled vs. measured ε_p values for the haptophyte *E. huxleyi* **(a)** Measured ε_p values from nitrate-limited chemostat cultures (Bidigare et al., 1997; Wilkes et al., 2018). **(b)** Modeled ε_p values, with $\gamma = 1.8$ and $\omega = 1.0$. **(c)** Comparison of modeled vs. measured ε_p values from (a) and (b). **(d)** Measured ε_p values from nutrient-replete batch cultures (Riebesell et al., 2000b; Rost et al., 2002). **(e)** Modeled ε_p values with $\gamma = 4.5$ and $\omega = 0.70 - 0.99$ (listed in the legend). **(f)** Comparison of modeled vs. measured ε_p values from (d) and (e). The horizontal dashed lines correspond to $\varepsilon_{\text{RubisCO}} = 11.1\text{‰}$ (*in vitro*; Table 1). Results are detailed in Table S9.

Figure 7. Modeled vs. measured ε_p values for *Alexandrium* dinoflagellate species **(a)** Measured ε_p values from nitrate-limited chemostat cultures (Hoins et al., 2016; Wilkes et al., 2017). **(b)** Modeled ε_p values, with $\gamma = 1.02$ and $\omega = 1.0$. **(c)** Comparison of modeled vs. measured ε_p values from (a) and (b). The linear fit omits the two outliers (circled). **(d)** Measured ε_p values from nutrient-replete batch cultures (Hoins et al., 2015). **(e)** Modeled ε_p values with $\gamma = 4.3$ and $\omega = 0.99$. **(f)** Comparison of modeled vs. measured ε_p values from (d) and (e), omitting the two outliers circled in (a). The horizontal dashed lines correspond to $\varepsilon_{\text{RubisCO}} = 19.5\text{‰}$ (*in vitro*; Table 1). Results are detailed in Table S9.

Figure 8. Modeled vs. measured ε_p values for the diatom *P. glacialis*. **(a)** Measured ε_p values from nitrate-limited chemostat cultures (Popp et al., 1998). **(b)** Modeled ε_p values, with $\gamma = 30$ and $\omega = 1.0$. **(c)** Comparison of modeled vs. measured ε_p values from (a) and (b). Results are detailed in Table S9.

Figure 9. Modeled vs. measured ε_p values for all taxa and conditions ($n = 140$). This fit omits the two dinoflagellate data points (circled in Figure 7).

Journal Pre-proofs

Tables & Figures

Table 1. Compiled $\epsilon_{\text{RubisCO}}$ and ϵ_f values for different RubisCO forms.

RubisCO Form	Biological Source	Organism Type	$\epsilon_{\text{RubisCO}}$ (‰) (<i>in vitro</i>)	Reference	ϵ_f (‰) (<i>in vivo</i>)	Reference
IA	<i>Solemya velum</i> symbiont	γ -Proteobacterium	24.5	Scott <i>et al.</i> (2004)	–	
	<i>Prochlorococcus marinus</i> MIT9313	Cyanobacterium	24	Scott <i>et al.</i> (2007)	–	
	<i>Synechococcus sp.</i>	Cyanobacterium	–	–	17	Popp <i>et al.</i> (1998)
IB	<i>Spinacia oleracea</i>	Higher Plant	26–30	Roeske & O’Leary (1984); Guy <i>et al.</i> (1993); Scott <i>et al.</i> (2004); McNevin <i>et al.</i> (2006)	–	
	<i>Gossypium</i>	Higher Plant	27.1	Wong <i>et al.</i> (1979)	–	
	<i>Nicotiana tabacum</i>	Higher Plant	27.4	McNevin <i>et al.</i> (2007)	–	
	<i>Synechococcus</i> PCC 6301 ^a	Cyanobacterium	21–22	Guy <i>et al.</i> (1993); McNevin <i>et al.</i> (2007)	–	
ID	<i>Emiliania huxleyi</i>	Coccolithophore	11.1	Boller <i>et al.</i> (2011)	25	Bidigare <i>et al.</i> (1997)
	<i>Skeletonema costatum</i>	Diatom	18.5	Boller <i>et al.</i> (2015)	–	
	<i>Phaeodactylum tricorutum</i>	Diatom	–	–	25	Laws <i>et al.</i> (1997)
	<i>Porosira glacialis</i>	Diatom	–	–	25	Popp <i>et al.</i> (1998)
II	<i>Riftia pachyptila</i> symbiont	γ -Proteobacterium	19.5	Robinson <i>et al.</i> (2003)	–	
	<i>Rhodospirillum rubrum</i>	α -Proteobacterium	18–23	Roeske & O’Leary (1985); Guy <i>et al.</i> (1993); McNevin <i>et al.</i> (2007)	–	
	<i>Alexandrium tamarense</i>	Peridinin-containing Dinoflagellate	–	–	27	Wilkes <i>et al.</i> (2017)

^a Freshwater cyanobacterium. PCC 6301 is a strain synonym for *Anacystis nidulans* and *Synechococcus* PCC 6301.

Figure Captions

Figure 1. Comparison of $\epsilon_{\text{RubisCO}}$ values measured *in vitro* with ϵ_f values determined *in vivo*. The data show the $\sim 25\text{‰}$ intercept (ϵ_f values) that result from plotting ϵ_p as a function of $\mu/[\text{CO}_{2(\text{aq})}]$ for eukaryotic phytoplankton grown in nitrate-limited chemostats. Lines represent geometric mean regression analysis. Black squares indicate the diatom *Phaeodactylum tricornutum* (Form ID RubisCO; Laws et al., 1997); dark grey triangles, calcifying and non-calcifying clones of the coccolithophore *Emiliania huxleyi* (Form ID RubisCO; Bidigare et al., 1997); light grey circles, dinoflagellate *Alexandrium tamarense* (Form II RubisCO; Wilkes et al., 2017); white diamonds, diatom *Porosira glacialis* (Form ID RubisCO; Popp et al., 1998). Ranges of $\epsilon_{\text{RubisCO}}$ measured *in vitro* (purified enzyme) are shown on the left side of the figure for RubisCO forms IA, IB, ID, and II (data, Table 1), with boxes shaded to correspond to the most similar chemostat-grown species.

Figure 2. Model structure. Dashed arrows indicate passive (diffusive) fluxes, thick solid arrows indicate either active transport processes or enzymatic conversions, and thin solid arrows indicate uncatalyzed chemical conversions. The invoked enzymes are RubisCO, carbonic anhydrase (CA), and a putative enzyme or other non-enzymatic process catalyzing the active hydroxylation of CO_2 to HCO_3^- (HYD). The interaction of photons with the thylakoid membrane is shown with a jagged arrow near the process of hydroxylation.

Figure 3. Net fluxes and isotopic compositions as a function of ω . (a-e) Carbon fluxes for a generic algal cell for the five (μ/CO_2) conditions highlighted in blue in Figure S3; C = CO_2 ; H = HCO_3^- . The cell is assumed to have an $\epsilon_{\text{RubisCO}}$ value of 11‰. The parameter γ , governing active bicarbonate uptake, is uniformly assigned a value of 1.5 (except for case (c), in which $\gamma = 10$). The arrow widths and directions are scaled to represent net fluxes, with wider arrows corresponding to larger fluxes. Dotted grey arrows are

used to represent non-zero fluxes that are several orders of magnitude smaller than the thinnest black arrows. The relative isotopic compositions and CO₂ concentrations of the carbon pools are illustrated with the shading of each carbon pool or cellular compartment: darker blue corresponds to a higher degree of ¹³C enrichment and darker grey corresponds to a higher [CO_{2(aq)}]. Interconversion of CO₂ and HCO₃⁻ by CA is bidirectional; here the unidirectional arrows (*e.g.*, H_c→C_c) show only the net, not gross, fluxes. Gross fluxes are depicted in Supplementary Figure S4. **(f)** ε_p vs. μ/CO₂ outcomes for cases **a-e**.

Figure 4. Behavior of the generalized model for *A. tamarensis* (a, b, c) and *E. huxleyi* (d, e, f). Panels show the model sensitivity to parameters ω, γ, P_C, P_H, and empirical inputs representative of each taxon. The dinoflagellate *A. tamarensis* was modeled with ε_{RubisCO} = 19.5‰, SA = 4300 μm², V = 26500 μm³, POC = 3500 pg C cell⁻¹, and default membrane permeability coefficients of P_C = 2.70×10⁻² cm s⁻¹ and P_H = 1.4×10⁻⁵ cm s⁻¹; [CO_{2(aq)}] was varied from 0.25 to 150 μmol kg⁻¹ and μ_i was uniformly assumed to equal 0.1 d⁻¹. The coccolithophore *E. huxleyi* was modeled with ε_{RubisCO} = 11.1‰, SA = 88 μm², V = 77 μm³, POC = 8.3 pg C cell⁻¹, and default membrane permeability coefficients of P_C = 0.85×10⁻² cm s⁻¹ and P_H = 1.4×10⁻⁵ cm s⁻¹; [CO_{2(aq)}] was varied from 0.5 to 100 μmol kg⁻¹ and μ_i was uniformly assumed to equal 0.4 d⁻¹. **(a, d)** Influence of the parameter γ, controlling the flux of actively imported HCO₃⁻: high γ = 4.5 (solid lines) for both taxa vs. low γ = 3 for *A. tamarensis* and 1.8 for *E. huxleyi* (dashed lines). **(b, e)** All cell and culture parameters are identical to (a, d), except γ is held constant at the taxon-specific “low” value and membrane permeabilities to CO₂ are varied: high P_C = 2.70×10⁻² cm s⁻¹ (solid lines) or low P_C = 0.85×10⁻² cm s⁻¹ (dashed lines). **(c, f)** All cell and culture parameters are identical to (b, e), except membrane permeabilities to HCO₃⁻ are varied: high P_H = 1.4×10⁻⁵ cm s⁻¹ (solid lines) or low (default; Table S1) P_H = 1.4×10⁻⁶ cm s⁻¹ (dashed lines).

Figure 5. Modeled vs. measured ϵ_p values for the diatom *P. tricornutum*. (a) Measured ϵ_p values from nitrate and phosphate-limited chemostat cultures (Cassar, 2003; Laws et al., 1997) (b) Modeled ϵ_p values, with $\gamma = 3.8$ and $\omega = 1.0$. (c) Comparison of modeled vs. measured ϵ_p values from (a) and (b). (d) Measured ϵ_p values from nutrient-replete batch cultures (Riebesell et al., 2000a; Burkhardt et al., 2000a,b). (e) Modeled ϵ_p values with $\gamma = 5.0$ and $\omega = 0.04 - 0.89$ (listed in the legend). (f) Comparison of modeled vs. measured ϵ_p values for (d) and (e). The horizontal dashed lines correspond to $\epsilon_{\text{RubisCO}} = 18.5\text{‰}$ (*in vitro*; Table 1). Results are detailed in Table S9.

Figure 6. Modeled vs. measured ϵ_p values for the haptophyte *E. huxleyi* (a) Measured ϵ_p values from nitrate-limited chemostat cultures (Bidigare et al., 1997; Wilkes et al., 2018). (b) Modeled ϵ_p values, with $\gamma = 1.8$ and $\omega = 1.0$. (c) Comparison of modeled vs. measured ϵ_p values from (a) and (b). (d) Measured ϵ_p values from nutrient-replete batch cultures (Riebesell et al., 2000b; Rost et al., 2002). (e) Modeled ϵ_p values with $\gamma = 4.5$ and $\omega = 0.70 - 0.99$ (listed in the legend). (f) Comparison of modeled vs. measured ϵ_p values from (d) and (e). The horizontal dashed lines correspond to $\epsilon_{\text{RubisCO}} = 11.1\text{‰}$ (*in vitro*; Table 1). Results are detailed in Table S9.

Figure 7. Modeled vs. measured ϵ_p values for *Alexandrium* dinoflagellate species (a) Measured ϵ_p values from nitrate-limited chemostat cultures (Hoins et al., 2016; Wilkes et al., 2017). (b) Modeled ϵ_p values, with $\gamma = 1.02$ and $\omega = 1.0$. (c) Comparison of modeled vs. measured ϵ_p values from (a) and (b). The linear fit omits the two outliers (circled). (d) Measured ϵ_p values from nutrient-replete batch cultures (Hoins et al., 2015). (e) Modeled ϵ_p values with $\gamma = 4.3$ and $\omega = 0.99$. (f) Comparison of modeled vs. measured ϵ_p values from (d) and (e), omitting the two outliers circled in (a). The horizontal dashed lines correspond to $\epsilon_{\text{RubisCO}} = 19.5\text{‰}$ (*in vitro*; Table 1). Results are detailed in Table S9.

Figure 8. Modeled vs. measured ε_p values for the diatom *P. glacialis*. (a) Measured ε_p values from nitrate-limited chemostat cultures (Popp et al., 1998). (b) Modeled ε_p values, with $\gamma = 30$ and $\omega = 1.0$. (c) Comparison of modeled vs. measured ε_p values from (a) and (b). Results are detailed in Table S9.

Figure 9. Modeled vs. measured ε_p values for all taxa and conditions ($n = 140$). This fit omits the two dinoflagellate data points (circled in Figure 7).

Figure 1

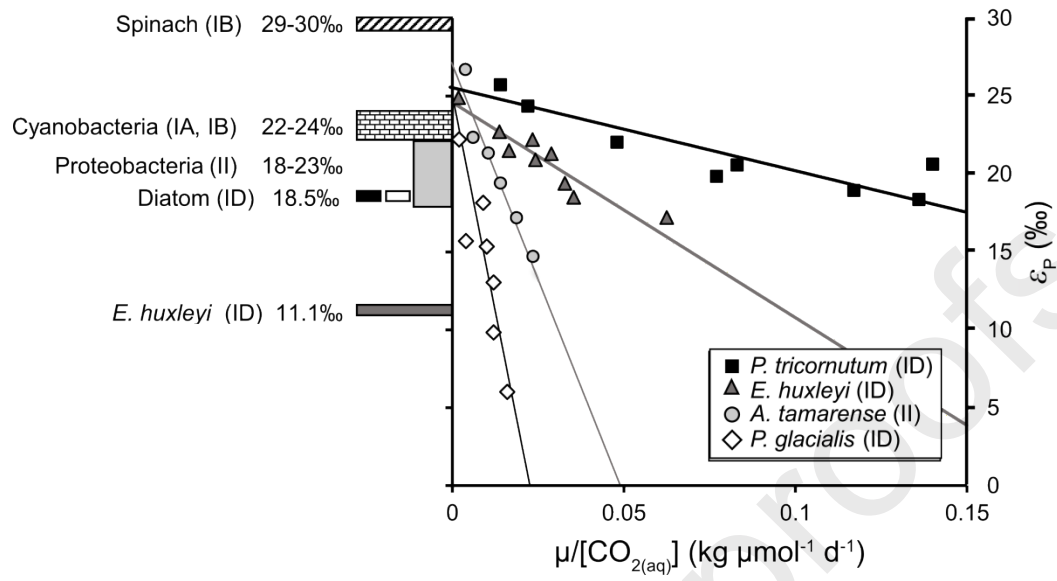


Figure 2

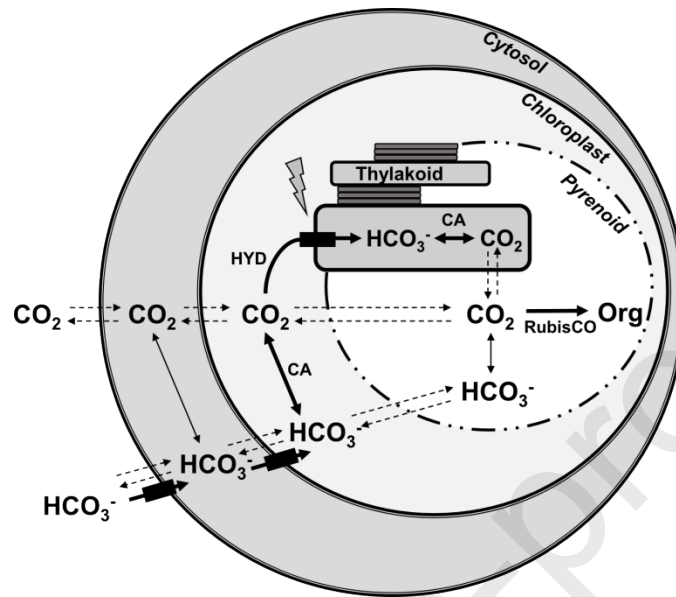


Figure 3

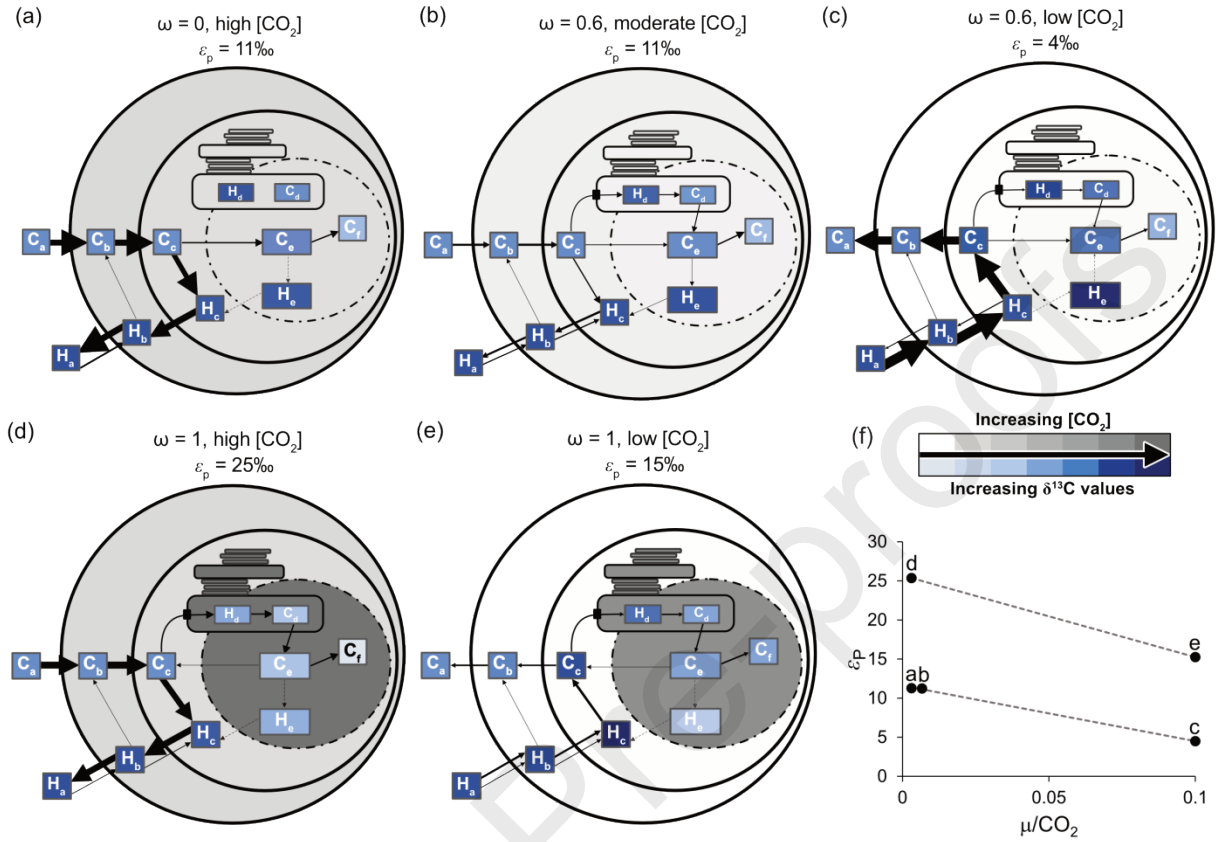


Figure 4

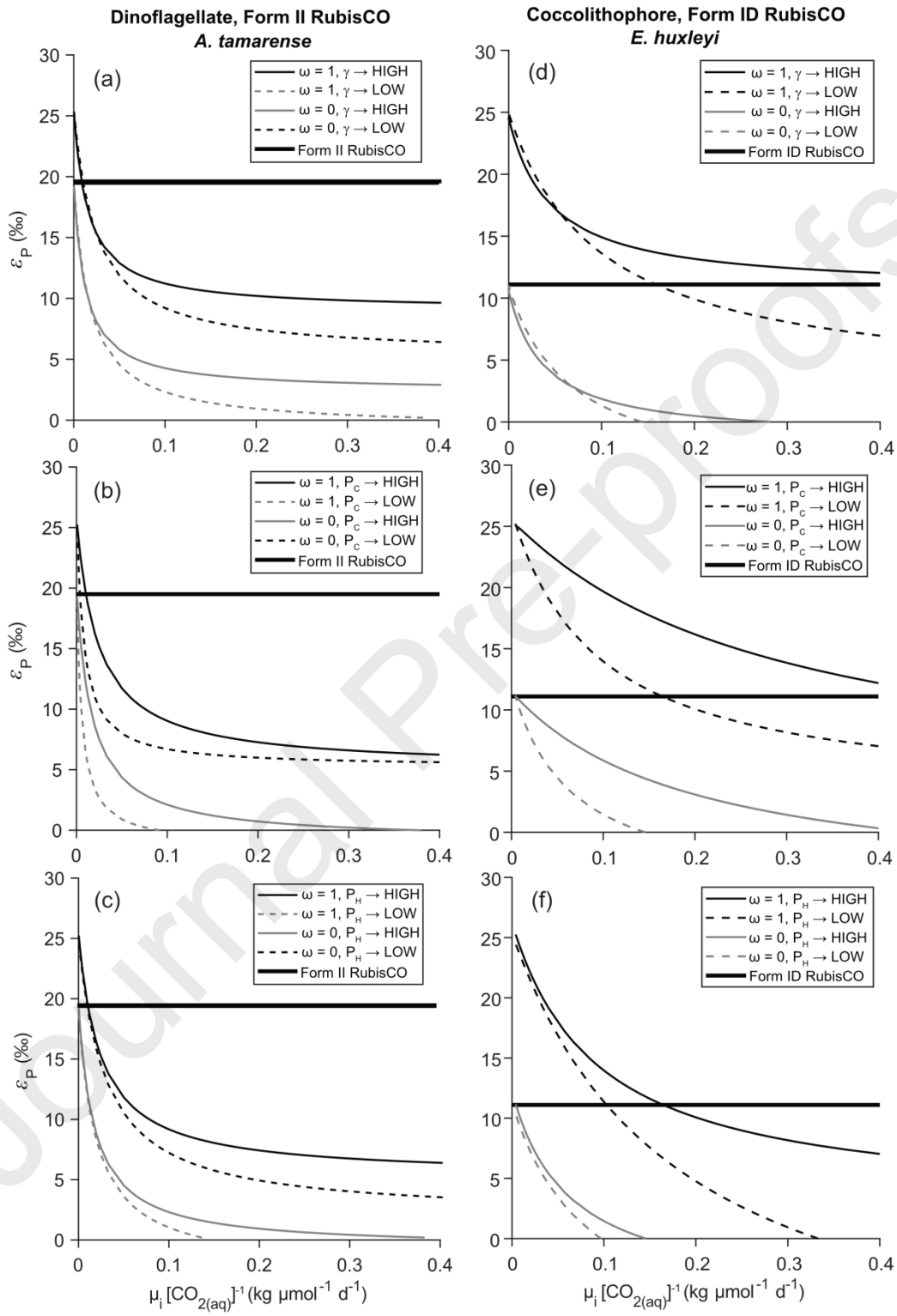


Figure 5

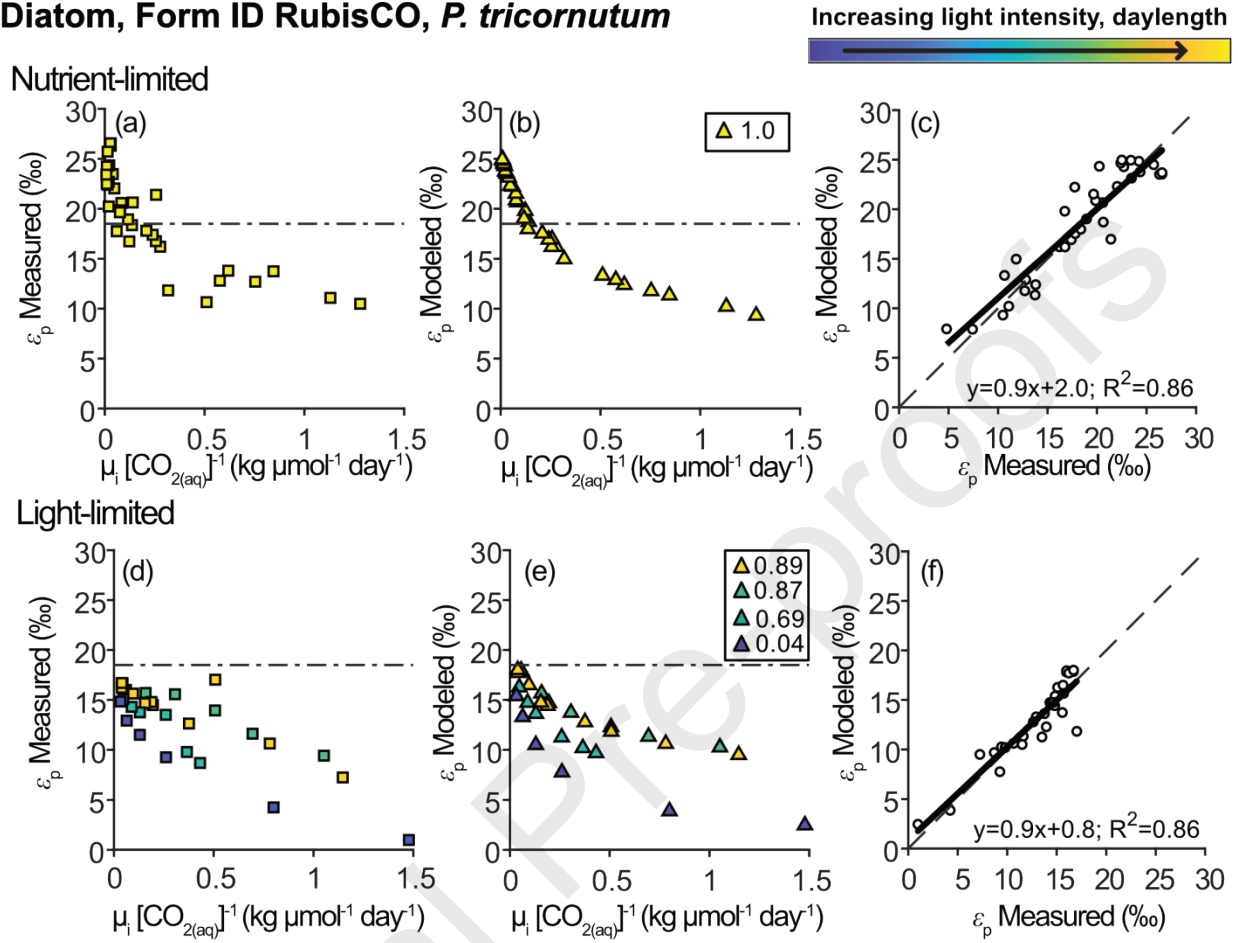
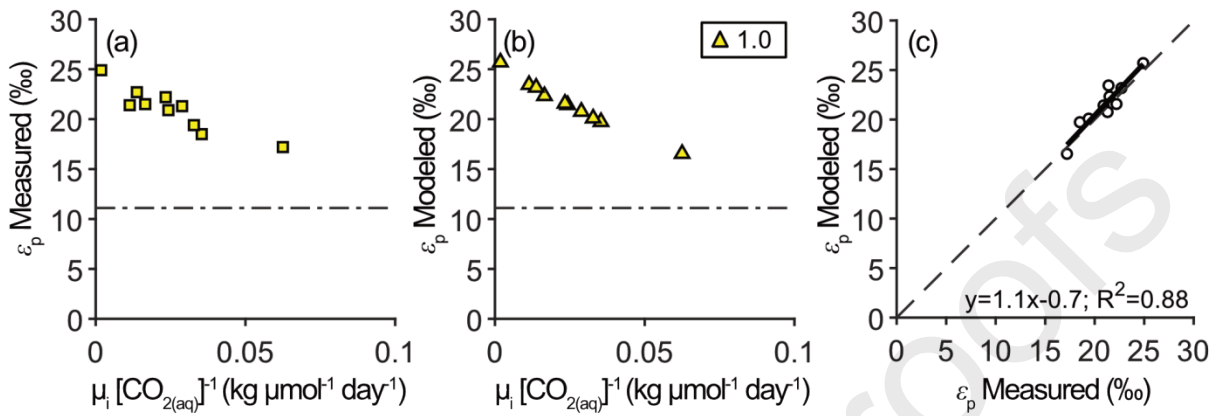
Diatom, Form ID RubisCO, *P. tricornutum*

Figure 6

Coccolithophore, Form ID RubisCO, *E. huxleyi*

Increasing light intensity, daylength

Nutrient-limited



Light-limited

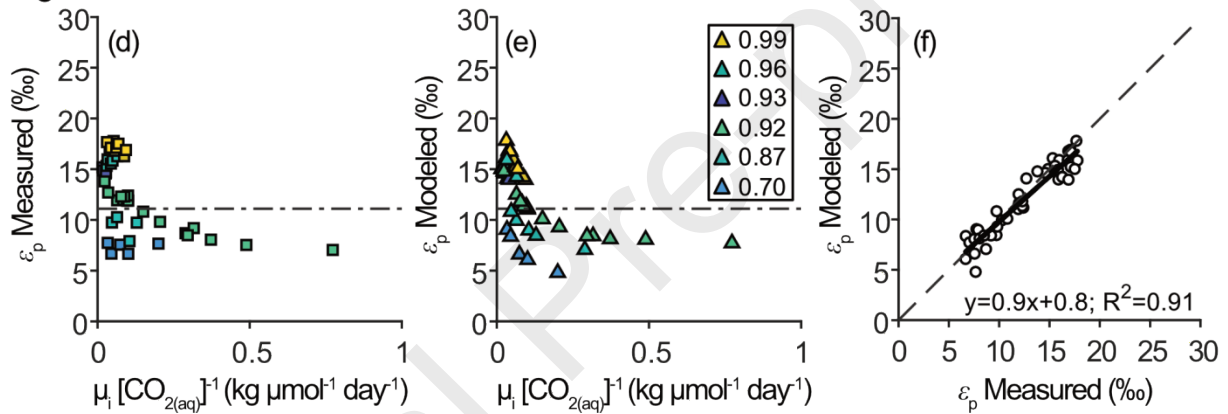
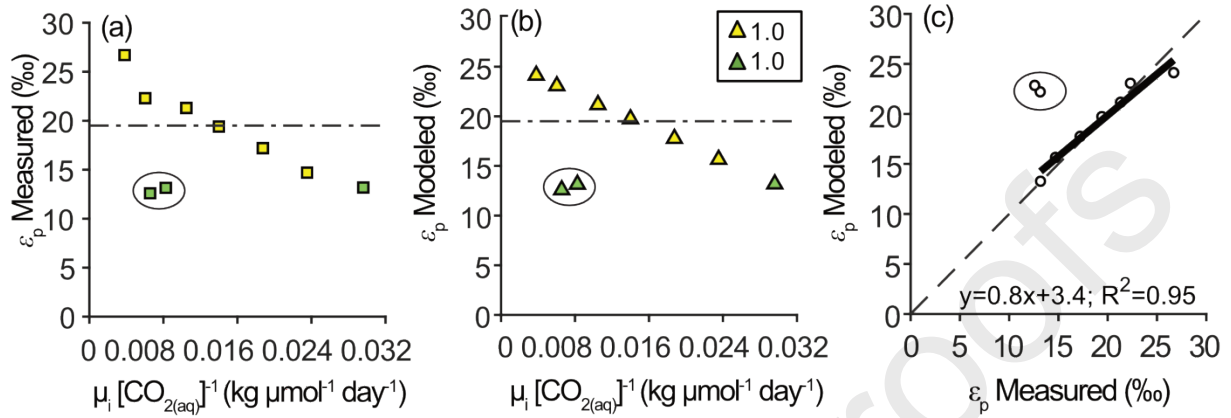


Figure 7

Dinoflagellate, Form II RubisCO, *A. tamarensis*

Increasing light intensity, daylength

Nutrient-limited



Light-limited

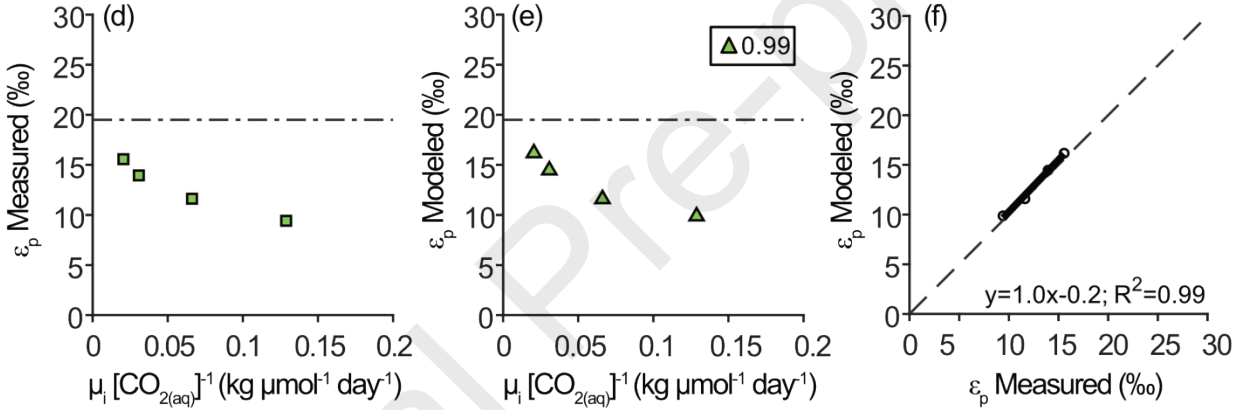


Figure 8

Diatom, Form ID RubisCO, *P. glacialis*

Nutrient-limited

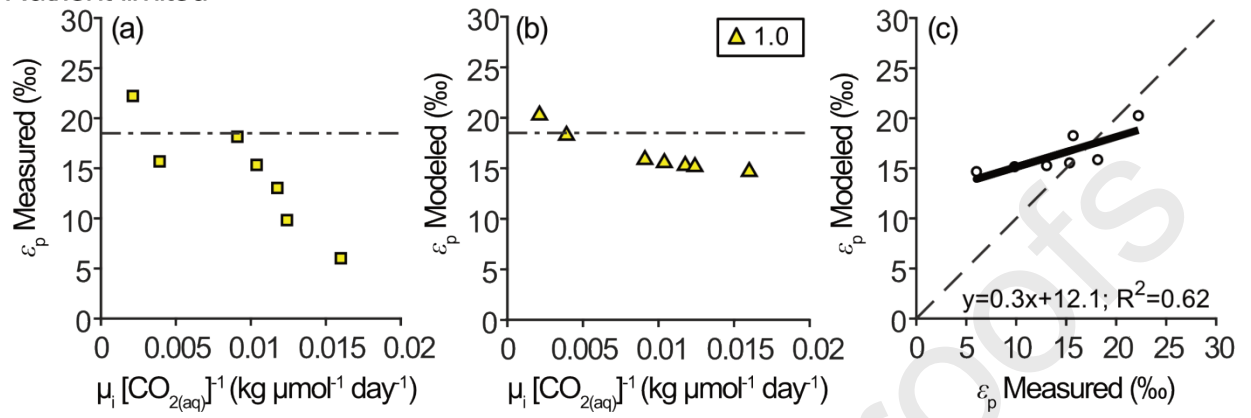


Figure 9

